AIAA JOURNAL
Vol. 54, No. 2, February 2016

Investigation of the Unsteady Flow and Noise Generation in a Slat Cove

M. Terracol* and E. Manoha†
ONERA–The French Aerospace Lab, 92320 Châtillon, France
and
B. Lemoine‡
École Centrale de Lyon, 69134 Lyon, France

DOI: 10.2514/1.J053479

This study presents hybrid Reynolds-averaged Navier–Stokes/large-eddy simulations of the unsteady flow and noise-generation phenomena in the slat cove of a high-lift wing profile. These computations are part of a joint numerical/experimental aeroacoustics collaborative program dedicated to slat-flow analysis. A dedicated two-element wing profile (slat plus main body) has been designed to isolate slat noise from other possible sources (e.g., the flap), while minimizing mean flow deflection effects, to improve the fidelity of open-jet wind-tunnel measurements. The design of this two-element airfoil has been performed numerically, using an optimization process based on steady Reynolds-averaged Navier–Stokes calculations. This airfoil has been investigated experimentally at the École Centrale de Lyon open jet facility. Unsteady zonal hybrid Reynolds-averaged Navier–Stokes/large-eddy simulations have been performed to provide a comprehensive description of the unsteady flow inside the slat cove, focusing on the noise-generation processes. A detailed analysis of the physics of the unsteady flow inside the slat cove is presented as well as a comparison of numerical results with available experimental data. The pressure spectra associated with the slat-cove flow are characterized by several tonal peaks emerging from the underlying broadband content. The existence of such peaks is attributed to a feedback loop involving the main shear layer inside the slat cove. A theoretical law is proposed to predict the associated tonal frequencies and assessed at the end of the paper.

Nomenclature

C_p	=	pressure coefficient
$\mathcal{C}(\xi,\tau)$	=	two-point/two-time correlation coefficient
c	=	retracted chord of the airfoil, m
c_s	=	slat chord, m
c_0	=	sound speed, m/s
D	=	mean cavity depth, m
f	=	frequency, Hz
f_n	=	feedback loop frequency, Hz
f_0	=	main shear-layer most-unstable frequency, Hz
I_1, I_2	=	indicators used for optimization
L_a	=	distance between the slat cusp and the reattachment point of the main shear layer, m
L_v	=	curvilinear length of the main shear layer, m
L_z	=	spanwise extent, m
$\mathcal{M}$	=	freestream Mach number
$\mathcal{N}$	=	Navier–Stokes operator
N_{xyz}	=	total number of grid cells
n	=	mode number
n_a	=	number of acoustic fronts
n_v	=	number of vortices
p	=	pressure, Pa
Q	=	Q criterion, s^{-2}
q	=	heat flux vector, W/m^2
Re	=	Reynolds number
$\mathcal{T}_L$	=	subgrid terms
t	=	time, s
$\boldsymbol{U}$	=	$(\rho, \rho u, \rho v, \rho w, \rho E)^T$, conservative variables vector
U_a	=	mean velocity inside the slat cove, m/s
U_v	=	mean convection velocity in the main shear layer, m/s
U_∞	=	freestream velocity, m/s
$U_\perp$	=	effective velocity measured by the hot wire, m/s
u	=	streamwise component of velocity, m/s
$\boldsymbol{u}$	=	$(u, v, w)^T$ velocity vector
v	=	vertical component of velocity, m/s
w	=	spanwise component of velocity, m/s
x, y, z	=	spatial coordinates, m
y_{TE}	=	vertical position of the trailing edge, m
α	=	angle of attack, deg
α_l	=	ratio L_v/L_a
Δ_z	=	spanwise grid resolution, m
δ_0	=	main shear-layer initial vorticity thickness, m
κ_a, κ_v	=	nondimensional velocities associated with U_a and U_v, respectively
λ_a	=	acoustic wavelength, m
λ_v	=	distance between two vortices, m
ξ	=	space interval, m
ρ	=	density, kg/m^3
ρE	=	total energy density, J/m^3
σ	=	viscous stress tensor, $kg \cdot m/s^2$
τ	=	time interval, s
Ω	=	physical domain of integration, m^3

Subscripts

ref	=	reference three-element solution
RMS	=	root mean square
SGS	=	subgrid scale

Presented as Paper 2011-3203 at the 20th AIAA Computational Fluid Dynamics Conference, Honolulu, HI, 27–30 June 2011; received 26 September 2014; revision received 24 August 2015; accepted for publication 1 September 2015; published online 22 December 2015.

*Doctor, Senior Research Scientist, Department of Aeroacoustics, 29 Avenue de la Division Leclerc.

†Doctor, Senior Research Scientist, Head of the Computational Aeroacoustics Research Unit, Department of Aeroacoustics, 29 Avenue de la Division Leclerc.

‡Ph.D. Student, Centre Acoustique, 36Avenue Guy de Collongue, Ecully Cedex; currently Doctor, Research Scientist, Institut de Recherche Mathématique de Rennes, University of Rennes 1, Campus Beaulieu, 35042 Rennes, France.

I. Introduction

THE reduction of airframe noise is currently a very important issue for aircraft manufacturers due to the constant increase in air traffic and to increasingly drastic constraints on the noise exposure levels. Because of the continued efforts in reducing engine noise, airframe noise becomes a significant contributor to the overall noise of the plane, especially in approach and landing configurations. Among the different noise sources, the high-lift devices (slat and flap) that are deployed to increase the global lift of the plane at low speeds have been identified as a major contributor to the overall noise. More specifically, the cove region between the deployed slat and the main wing appears as a preponderant source of noise. Thus, it becomes of outstanding importance to develop numerical and experimental approaches capable not only of predicting the noise generated by such devices, but also of understanding the main physical phenomena responsible for noise generation, to propose active or passive noise control solutions.

Numerous studies have been performed in that direction, both in the numerical and experimental domains. The growing computational resources capabilities have led to an increase in the prediction capabilities of unsteady turbulence-resolving numerical methods. Such approaches therefore provide a fine analysis tool for a better understanding of the physical mechanisms involved in the noise-generation process. Since the pioneering works of Khorrami et al. [1] using an unsteady Reynolds-averaged Navier–Stokes (RANS) strategy, several works have therefore been performed, using large-eddy simulation (LES) [2,3], zonal hybrid RANS/LES methods [4–7], or global hybrid RANS/LES methods [3,6,8–14].

Several experimental works have also been performed to study slat noise [15–20]. These works are very useful to provide general trends and provide reliable databases to assess the simulations. However, the available experimental data are often limited to a statistical analysis of the flow and/or far-field noise measurements. Thus, it appears to be of crucial interest to combine the respective advantages of the two available approaches by developing joint experimental/numerical programs.

The experimental study of slat noise is very difficult because the test setup must fulfill both aerodynamic and acoustic requirements, which are generally contradictory. From the aerodynamic point of view, it is necessary to generate a mean flow around the slat that is as close as possible to the flow under infinite conditions, which generally requires testing a complete three-element configuration (slat, main wing, and flap) in a closed-section aerodynamic wind tunnel. However, such wind tunnels are generally not suitable for acoustic measurements because they are noisy and nonanechoic. On the other hand, from the acoustic point of view, it is much preferable to work in an open-jet, anechoic, and silent wind tunnel. However, a conventional three-element wing generates a very high lift that is able to strongly deflect the open jet of the wind tunnel, with two consequences from both the aerodynamic and acoustic points of view.

1) Aerodynamics: the mean flow around the airfoil is distorted and no longer representative of the flow under infinite conditions. In particular, it is always necessary to modify (increase) the airfoil global incidence in the wind tunnel, to get closer to the targeted pressure distribution predicted by computational fluid dynamics (CFD) computations achieved under infinite conditions.

2) Acoustics: because of its deviation by the airfoil lift, the wind-tunnel jet impinges the collector with a bad incidence, increasing the wind-tunnel background noise and possibly damaging the structure. Moreover, the presence of the deployed trailing-edge flap adds flow noise sources that complicate the study of slat noise.

For these reasons, the first objective of this study was to design an airfoil with the following requirements.

1) The flow (streamlines, velocity amplitudes, wall pressure distribution, and turbulent kinetic energy distribution) in the slat cove should be representative of low-speed (approach) flight conditions, with a given classical three-element configuration at moderate global incidence.

2) The overall wing lift and mean flow deflection by the airfoil should be minimized.

3) The slat-noise sources should be isolated from other possible flow noise sources.

These requirements have led to the development of a "slat-only" airfoil configuration. The first objective of this study is therefore to design a dedicated two-dimensional model suitable for a reliable experimental study of slat noise to be performed in the aeroacoustic open-jet wind tunnel of the École Centrale de Lyon (ECL). This database has been used in the FP7 European project Validation and Improvement of Airframe Noise Predition Tools (VALIANT) for further validation of the CFD/computational aeroacoustics (CAA) codes to predict slat noise. For that purpose, the idea was to start from an existing three-element airfoil, keep the upstream part of the airfoil (deployed slat and main wing leading edge), and generate a new downstream shape for the airfoil with a given chord and a sharp trailing edge (TE), without any deployed flap. This is performed in practice by using an optimization process in which the varying parameters are 1) the airfoil global incidence, and 2) the vertical position of the wing trailing edge. Using this optimization process, optimal values of these two parameters are derived to fulfill the previous requirements as well as possible. The optimization process as well as the optimal selected configuration are first presented in Sec. II.

This configuration has been studied experimentally in the École Centrale de Lyon anechoic wind tunnel. The associated experimental setup is briefly described in Sec. III.

The main contribution of this study is based on several unsteady numerical simulations of this two-element configuration. These simulations focus only on the slat-cove area using a zonal RANS/LES approach, the nonlinear disturbance equation (NLDE) method [4,21–23], which is briefly described and then applied to the selected configuration in Sec. IV. A fine physical analysis of the flow and noise-generation processes is performed on the basis of the numerical results; the main physical features of the flow and a statistical analysis are reported in Sec. IV.C. Then, an unsteady analysis of the flow is performed in Sec. IV.D. It is based on a spectral analysis of the main shear layer and of the wake of the upper trailing edge as well as on the wall pressure spectra inside the slat cove. A comparison between the numerical and experimental results is also performed.

The measured and computed pressure spectra appear to be characterized by narrowband peaks emerging from the broadband frequency content. A possible interpretation based on a cavity feedback loop of these tonal components is proposed in Sec. V as well as a theoretical prediction model for the associated discrete frequencies.

II. Definition of the Numerical/Experimental Setup: Optimization Approach

A. Reference Airfoil and Configuration

The reference airfoil is the FNG Airbus geometry, which was developed in the German Research & Technology (R&T) projects LuFo III and ProHMS between 2000 and 2003 and has been released for all R&T-related purposes. This airfoil has been widely used by the DLR, German Aerospace Center [24]; several models were built with various scales. The smaller one is called F16 and was built for the DLR aeroacoustic wind tunnel brunswick (AWB) aeroacoustic wind tunnel. Its retracted chord measures 300 mm, and its span is 800 mm. The three-element reference configuration of this F16 geometry corresponds to the slat/flap deployed at 28.814/38.296 deg (see Fig. 1). The two-dimensional (2-D) multiblock structured grid required for the calculation of this three-element configuration has

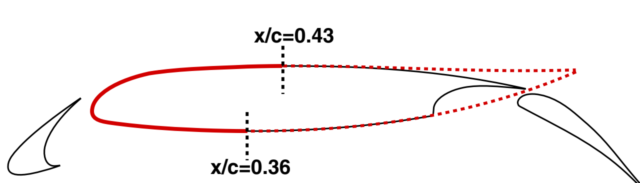

Fig. 1 Original F16 geometry (solid line) and optimized main wing element geometry (dashed line).

been built using MESH3D [25], which is an in-house parametric grid generator developed at ONERA–The French Aerospace Lab and is composed of approximately 180,000 cells. The flow conditions have been set to be 1) as close as possible to realistic landing flow conditions, 2) compatible with the École Centrale de Lyon wind-tunnel facility, and 3) still accessible for an unsteady turbulence-resolving numerical simulation. The selected flow conditions are 1) freestream Mach number $\mathcal{M} = 0.15$, 2) retracted chord of the airfoil $c = 300$ mm, and 3) angle of attack $\alpha = 4$ deg.

The associated chord-based Reynolds number of the problem is $Re = 1{,}047{,}000$. Figure 2 (left) shows mean flow streamlines for this reference configuration obtained using a steady RANS calculation. It is worth noting that this airfoil introduces significant flow deflection effects, both in the upstream and downstream directions, therefore making it inappropriate for open-jet wind-tunnel tests.

B. Generation of the Low-Lift Slat-Only Configuration

As stated in Sec. I, the first step of this study was to design a dedicated airfoil configuration, focused on slat-flow mechanisms and well suited for open-jet wind-tunnel tests. For that purpose, a two-element airfoil composed of a deployed slat and a main wing body has been designed, in such a way that 1) the flow in the slat-cove area remains representative of a real high-lift wing profile (i.e., similar to that of the reference three-element airfoil), and 2) the airfoil minimizes mean flow deflection effects and generates only a low lift.

1. Optimization Process

The global optimization process used for generating the two-element low-lift slat-only configuration can be recast as follows.

1) The first step of this process consists of specifying two free input parameters (angle of attack α and position of the trailing edge). The vertical trailing-edge position y_{TE} being imposed, a new shape is generated for the main body. Thus, a cubic spline reconstruction of the airfoil is performed, keeping the original node discretization of the leading-edge part of the main wing, which is kept identical to the reference three-element airfoil (see Fig. 1) and adding a new node at the new trailing-edge location. Based on this new definition, a new discretization of the shape is generated, to be used as input data for the grid generator. It must be noted that only the main wing element is modified, whereas the slat geometry is kept identical.

2) The second step then consists of generating a structured grid around this new airfoil, using the obtained shape discretization and the parametric grid generator MESH3D.

3) The RANS simulation is then run using this new mesh and the specified angle of attack. The results of the RANS simulation are then analyzed and compared to the targeted reference solution by calculating appropriate indicators. In this study, two specific indicators I_1 and I_2 have been selected. They are defined as follows:

$$I_1^2 = \iiint_{\Omega_{\mathrm{slat}}} (u - u_{\mathrm{ref}})^2 + (v - v_{\mathrm{ref}})^2 \,\mathrm{d}\Omega \quad \text{and}$$

$$I_2^2 = \iiint_{\Omega_{\mathrm{wake}}} (v/u - \tan(\alpha))^2 \,\mathrm{d}\Omega$$

where u and v denote the streamwise and vertical components of the velocity vector, respectively; the subscript "ref" refers to the reference three-element solution; the two domains Ω_{slat} and Ω_{wake} denote a domain located inside the slat cove and one in the vicinity of the airfoil trailing edge, respectively (see Fig. 3). Using these two definitions, I_1 represents a measure of the mean flow difference in the slat cove between the two-element airfoil and the reference three-element airfoil, whereas I_2 is a measure of the mean flow deflection by the two-element airfoil.

4) New input parameters (α and y_{TE}) are chosen to minimize the errors between the new solution and the targeted solution.

5) The process is restarted using this new set of input parameters until the errors reach an acceptable lower threshold.

2. Numerical Method

All of the computations presented in this study have been performed using the in-house ONERA CFD/CAA code FUNk on structured multiblock grids. This compressible solver handles several sets of equations: Euler, Navier–Stokes, filtered Navier–Stokes (LES), and Reynolds-averaged Navier–Stokes (RANS). These equations can be solved considering either a full variable or a perturbation formulation. The solver also incorporates zonal RANS/LES capabilities. Several subgrid models are available for LES: the Smagorinsky model, the selective mixed-scale model, the approximate deconvolution model, and mixed and multiscale deconvolution models. RANS equations are solved using the Spalart–Allmaras (SA) turbulence model. The solver allows several numerical schemes to be used: high-order (sixth-order) finite-difference schemes as well as finite-volume schemes [modified second-order advection upstream splitting method (AUSM+(P)] scheme with wiggle detector, Roe scheme) are available. Time integration can be performed using a second-order implicit backward Euler scheme (using a Newton subiteration process) or an explicit

Fig. 3 Integration domains used for the optimization process.

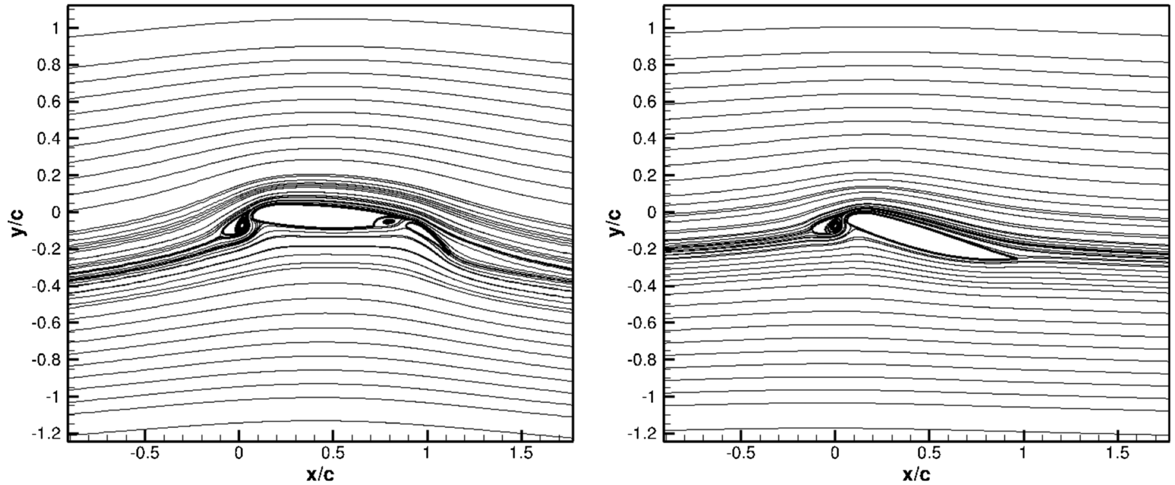

Fig. 2 Mean flow streamlines around the reference three-element airfoil (left) and optimized two-element airfoil (right).

Table 1 Computed lift and drag forces for the experimental span of 300 mm

Force (Newtons)	Two-element airfoil	Three-element airfoil
Lift (full airfoil)	127.46	364.83
Drag (full airfoil)	6.24	10.15
Lift (slat only)	17.15	20.90
Drag (slat only)	0.77	–6.40

third-order accurate compact Runge–Kutta scheme. Great care has been taken to ensure a very good efficiency of the solver on both massively parallel or vectorial supercomputers.

The optimization process used for this part of the study is based on steady RANS simulations, for which the Spalart–Allmaras turbulence model has been selected. For these steady flow simulations, the Roe scheme has been used for spatial discretization, whereas time integration has been performed using an implicit local time-stepping approach.

The optimization process itself is based on an external optimization software DAKOTA, developed at Sandia National Laboratories,[§] which makes it possible to automatically select a new set of optimization parameters $(\alpha; y_{\mathrm{TE}})$ from the evolution of the two indicators I_1 and I_2. However, first simulations have shown that using a too-wide parameter space for $(\alpha; y_{\mathrm{TE}})$ leads the optimization algorithm to an unacceptable local minimum for the error norms. Thus, it has been chosen to first perform a coarse exploration of the parameter space and to manually identify a reduced parameter space where the automatic optimization could be restarted. For this purpose, 114 RANS computations have been performed, with the angle of attack α varying from 4 to 22 deg, with a step of 1 deg, and the vertical position of the trailing-edge y_{TE} varying from 0 to $0.125c$, with a step of $0.025c$. Based on the error maps obtained, a reduced parameter space has been defined, and the automatic optimization process using DAKOTA has been restarted in this region. Convergence of the algorithm was then obtained after only 24 additional simulations.

3. Results: Optimized Two-Element Airfoil

After a total of 138 RANS calculations, an unconventional optimal configuration has been determined. It corresponds to the following set of parameters: $\alpha = 18$ deg and $y_{\mathrm{TE}}/c = 0.06$. Figure 2 shows a comparison between the three-element reference configuration and the optimized slat-only airfoil. It must be noted that the angle of attack used for the optimized configuration is considerably higher than that used for the reference configuration. Despite this, it can be observed that the optimized configuration leads to a significant reduction of the mean flow deflection effects, both in the downstream and upstream parts of the flow, thanks to the unconventional shape of the airfoil near the trailing edge. This point reveals a good performance of the optimized airfoil in minimizing deflection effects, which is a very good point for wind-tunnel tests. As a consequence, the lift applied on the airfoil is also significantly decreased. Table 1 compares the lift and drag forces of the two airfoils computed for the experimental span of 300 mm. The overall lift appears to be reduced by a factor of almost 3 for the two-element airfoil, whereas the overall drag is also decreased by about 38%. Although the lift force acting on the full airfoil is very significantly reduced, the lift force acting on the slat only is, however, only reduced by about 18%. This observation is consistent with the fact that the flow in the slat region is very similar between the optimized two-element airfoil and the original three-element one.

Figure 4 compares mean flow visualizations in the slat-cove area of the reference and optimized airfoils. Both flows look very similar in this region. This similarity in the slat region is also confirmed by looking at the pressure coefficient distributions presented in Fig. 5. It is also striking from this figure that the global lift of the airfoil is significantly decreased for the proposed two-element airfoil. Therefore, the flow in the slat of the optimized two-element airfoil appears representative of a realistic high-lift airfoil, whereas the global flow deflection and lift force are significantly decreased with respect to a conventional three-element airfoil, which makes it significantly more suitable for wind-tunnel tests.

III. Experimental Setup and Measurements

The experimental investigations were conducted at the Centre Acoustique of the École Centrale de Lyon, in the open-jet anechoic wind-tunnel. The anechoic chamber dimensions are 10 by 8 m, with a height of 8 m.The wind-tunnel exit duct has a square cross section, with sides measuring 0.56 m. A convergent nozzle has been added for the experiments, leading to a rectangular cross section 0.4 m wide by 0.3 m tall. Finally, two horizontal end plates fixed on the nozzle lips hold the investigated mockups mounted vertically. The sketch of the setup is shown in Fig. 6, together with two pictures of the airfoil. Brushes have also been installed along the downstream edges of the end plates to minimize spurious noise sources contaminating the low-frequency range.

Because of expected flow deflection effects, the angle of attack of the airfoil had to be tuned to match, as well as possible, the reference steady-state C_p distribution provided by freestream RANS calculations at $\alpha = 18$ deg. The optimal and selected value of the angle of attack for the measurements is finally 25 deg.

Inflow speeds ranging from 30 to 70 m/s have been tested, focusing on the reference speed of 50 m/s. Steady-state pressure measurements have been performed at several locations all along the airfoil. In addition to this, several unsteady pressure probes have been placed inside the slat cove on the slat surface and in the leading-edge region of the main wing element to perform unsteady wall pressure measurements. Fluctuations of the wall pressure are measured using the remote microphone probe (RMP) technology. The latter is a quasi-nonintrusive technology developed at ECL to measure wall-pressure fluctuations of any kind. A pinhole in the surface of the mockup with a diameter of 0.5 mm is the actual measuring point. The fluctuating pressure taken at that point then propagates as sound inside a capillary tube and is captured by a microphone located outside the mockup (here above the upper nozzle end plate). A correction is needed to compensate for the viscous attenuation and secondary reflections in the capillary. Usually, the calibration is achieved using a specific device made of a hollow cylinder connected to a small-size loudspeaker and to a reference microphone. The frequency response of the RMP with respect to this microphone is the basis for the procedure, and the end of the cylinder must be placed above the measuring orifice without any leakage. This cannot be ensured for highly curved walls like the ones of the slat cove and produces perturbations in the correction functions. Therefore, a theoretical frequency response based on the detailed description of the probe geometry, in terms of lengths and diameters of probe sections, has been substituted. Figure 7 illustrates the effect of this frequency-response function on the pressure spectrum for one measurement hole located on the slat surface inside the slat cove.

Single hot-wire probe measurements (Fig. 8) have also been used to access the mean-velocity profiles as well as velocity fluctuations in the local streamwise direction. This has also enabled the flow upstream of the mockup to be characterized in the two directions of the nozzle outlet. Velocity profiles are mainly measured in the transverse direction (normal to the incident flow) in the midspan plane. The meshing ranges from 0.5 mm close to the wall of the bodies to 100 mm farther away in the external flow. Only the nominal case at $\alpha = 25$ deg at the reference speed of 50 m/s has been investigated for this kind of test. Measurements in the nozzle outlet cross section also provided the flow characteristics (velocity profiles, turbulent rate, and homogeneity); a turbulence rate lower than 0.5% has been determined, based on the maximum mean-flow velocity.

Far-field pressure measurements have been performed using two B&K 1/2 in. microphones mounted in diametrically opposite positions on a rotating system. The support of each microphone has a length of 2 m, and the measurement plane fits with the setup midspan plane. Additional measurements have been performed by ONERA

[§]Data available online at https://dakota.sandia.gov [retrieved October 2009].

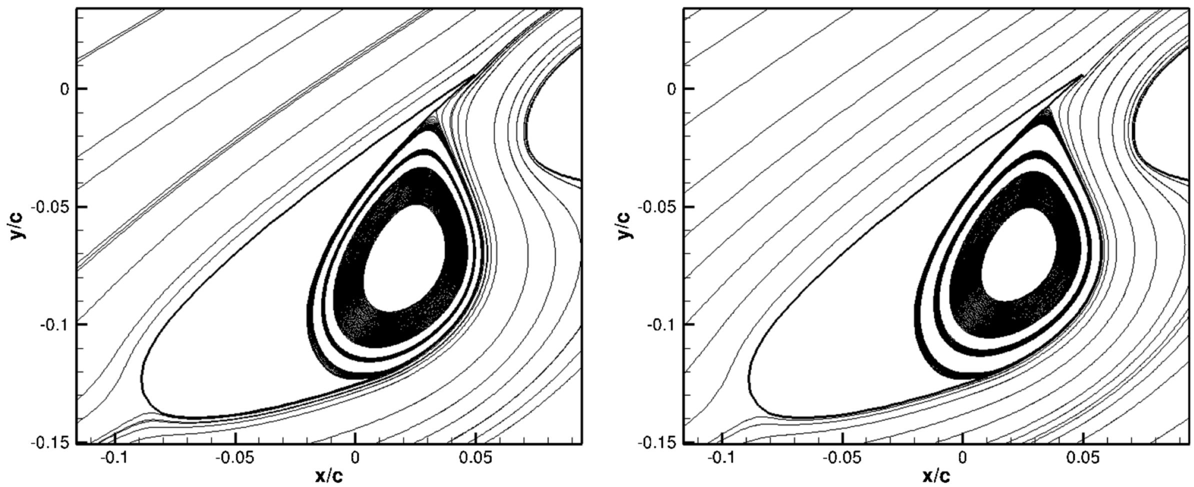

Fig. 4 Mean flow streamlines in the slat cove of the reference three-element airfoil (left) and optimized two-element airfoil (right).

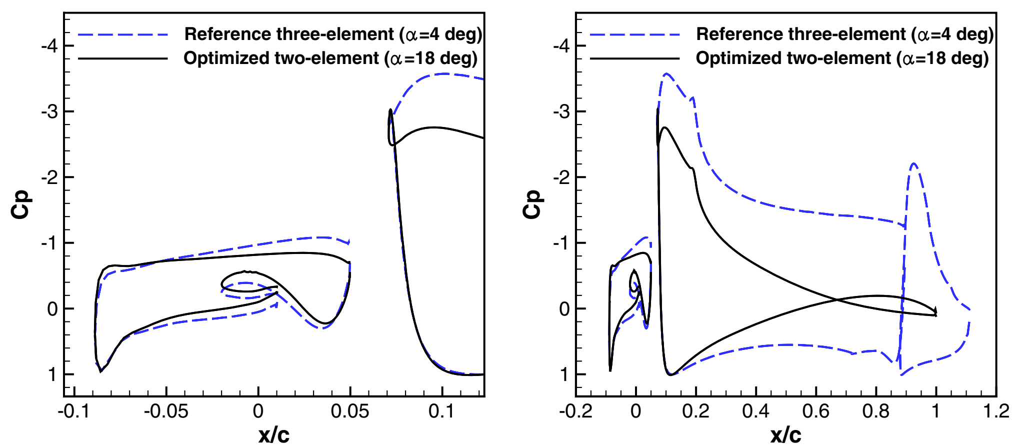

Fig. 5 Pressure coefficient distributions of the optimized two-element and reference three-element airfoils. Left: slat region; right: full airfoil.

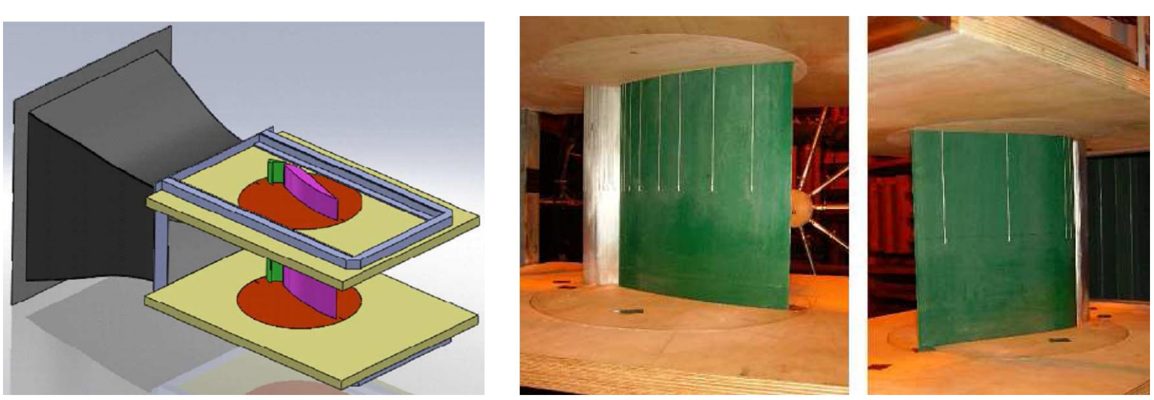

Fig. 6 Experimental setup.

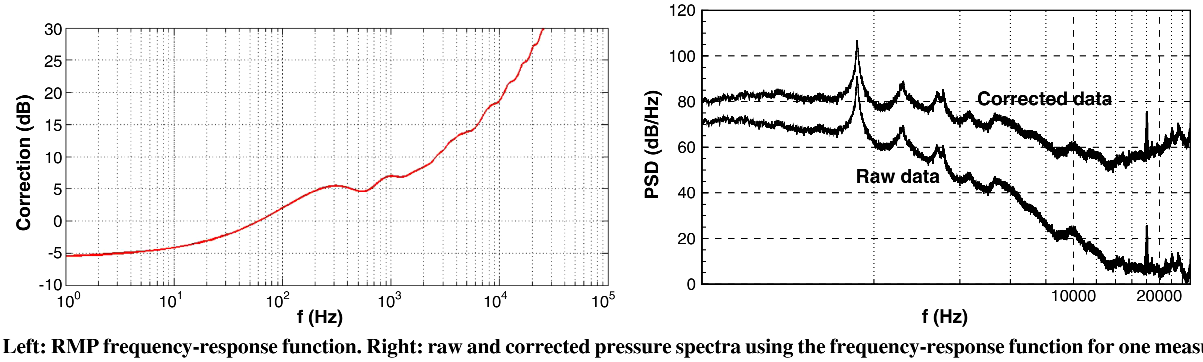

Fig. 7 Left: RMP frequency-response function. Right: raw and corrected pressure spectra using the frequency-response function for one measurement hole located on the slat surface inside the slat cove.

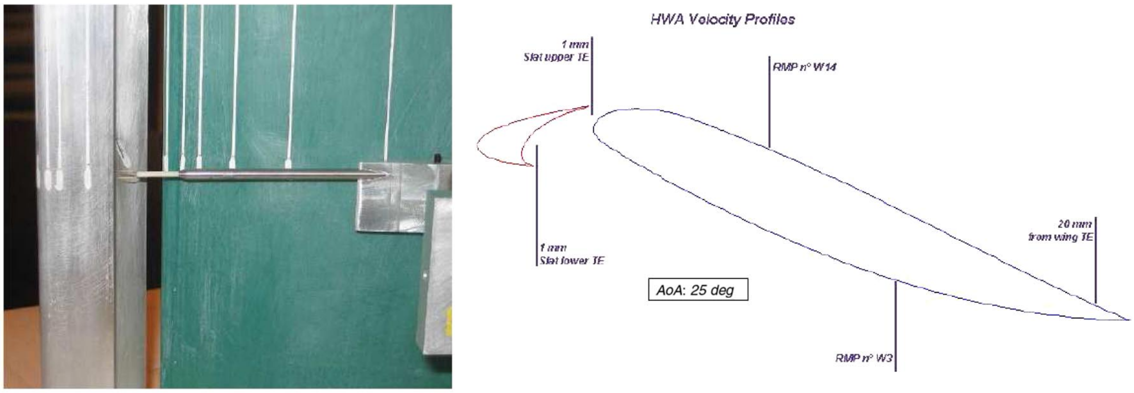

a) b)

Fig. 8 Single hot-wire anemometry probe: a) picture of the probe and its support, and b) measuring paths of the probe.

using a cross-shaped acoustic antenna with 109 B&K 1/4 in. microphones. The latter made it possible to perform source localization, which confirmed that the main acoustic source is located in the slat-cove region. Figure 9 displays the far-field pressure spectra measured by one microphone of the acoustic antenna, for different inflow speeds ranging from 30 to 70 m/s. It is worth noting that the spectra are characterized by the presence of several tonal peaks emerging from the broadband content. This point is discussed in Sec. V, where a possible physical interpretation is proposed, together with an analytical prediction model of the discrete frequencies. As can be observed in Fig. 10, the sensitivity of the amplitude of these tonal components to the airfoil angle of attack is rather high; for an inflow speed $U_\infty = 50\ \mathrm{m/s}$, an increase in the angle of attack of the airfoil from 25 to 27 deg results in an attenuation of about 6 dB of the amplitude of the main tonal peaks in the far-field pressure spectra. Such a behavior has also been observed in separate measurements performed on the original three-element F16 in the DLR AWB open-jet wind tunnel [26]. This can be observed in Fig. 11, which shows the measured far-field pressure spectra for the F16 airfoil under similar flow conditions. An increase by 4 deg of the angle of attack is observed, in this case, to yield to an attenuation between 6 and 10 dB of the main tonal peak amplitudes. This reveals that the response of the two-element designed airfoil to some changes in the angle of attack is qualitatively the same as that of the original three-element airfoil. Figure 12 presents a more quantitative comparison between the measured far-field pressure spectra of the optimized two-element airfoil and those from the original three-element F16 airfoil, taken from the LEISA2 experimental database [26]. Two values of the angle of attack, 10.5 and 14.5 deg, are plotted for the three-element airfoil because the reference angle of attack of 4 deg under free-field conditions is expected to be matched by a 12 deg angle of attack under AWB conditions, unfortunately not available for comparison. The spectra presented in this figure have been corrected to account for the differences between the experimental conditions (AWB and ECL wind tunnels). The corrections applied in each case therefore account for the shear-layer refraction and installation effects (end plates),

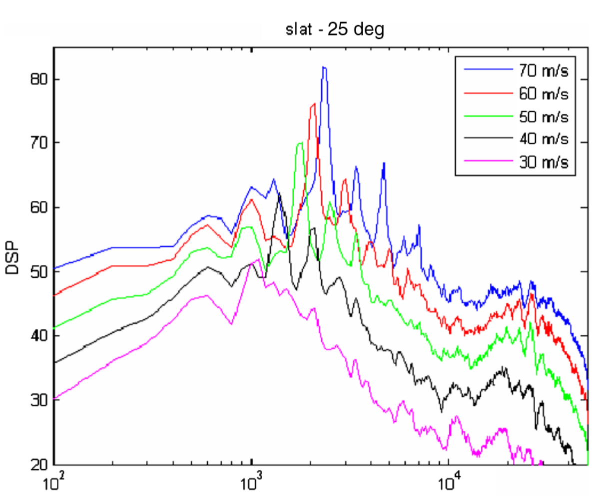

Fig. 9 Measured far-field pressure spectra at $\alpha = 25$ deg for different values of the inflow velocity.

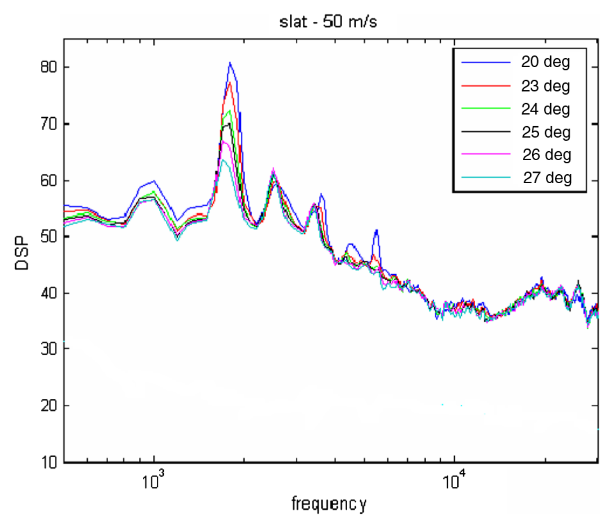

Fig. 10 Measured far-field pressure spectra at $U_\infty = 50\ \mathrm{m/s}$ for different values of the angle of attack.

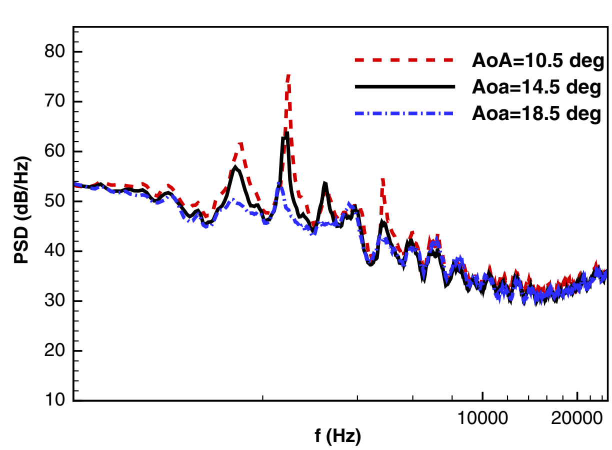

Fig. 11 Measured far-field pressure spectra for the original three-element F16 airfoil, in DLR AWB open-jet wind tunnel, at $U_\infty = 50\ \mathrm{m/s}$ for different values of the angle of attack.

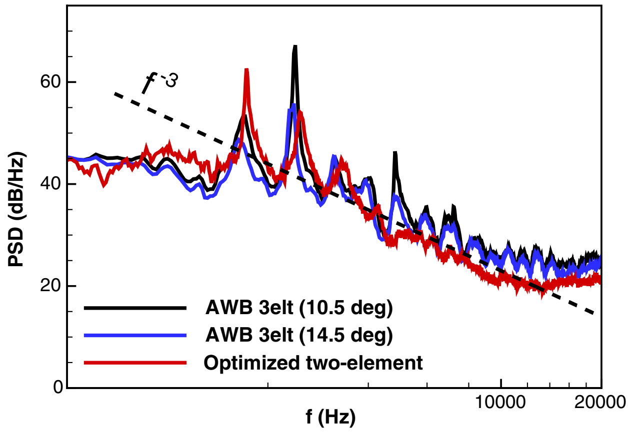

Fig. 12 Measured far-field pressure spectra for the original three-element F16 airfoil and for the optimized two-element airfoil, at $U_\infty = 50$ m/s (see text for details).

whereas the levels are normalized for a span of 1 m and an observer distance of 1 m. The equivalent observation angle under free-field conditions is 90 deg below the slat, with respect to the jet axis. It is clear from this comparison that the noise radiated by the optimized two-element airfoil is very similar to the one of the original three-element airfoil, although a perfect agreement is not completely obtained; all of the spectra are characterized by similar levels and decay rates, as well as by the presence of several tonal peaks, at similar frequencies. The proposed simplified two-element airfoil therefore appears as a reliable configuration for slat-noise analysis.

IV. Hybrid Simulation of the Slat Cove Area

A. Methodology

In the slat-cove region, the resolution is performed using a zonal RANS/LES approach, the NLDE [4,21–23] method, which is based on a decomposition of the flow between a mean field computed by RANS and turbulent fluctuations computed by LES in a reduced domain. Therefore, the original grid has been divided into two distinct regions, resolved either in pure RANS or in pure LES mode. The domain decomposition used in this case is detailed in Fig. 13 (grid points match one-to-one in the x-y plane between the RANS and NLDE domains).

The principle of the method is to decompose the conservative variable vector $\boldsymbol{U}$ as the sum of a mean part and a fluctuating part. The mean part $\langle \boldsymbol{U} \rangle$ can be computed using a classical RANS parameterization over the entire configuration, whereas the calculation of the fluctuating part $\boldsymbol{U}'$ is performed only locally using an LES-like formulation. This splitting therefore represents a triple decomposition of the full unsteady field $\boldsymbol{U}$ as

$$\boldsymbol{U} = \langle \boldsymbol{U} \rangle + \boldsymbol{U}' + \boldsymbol{U}_{\mathrm{SGS}} = \bar{\boldsymbol{U}} + \boldsymbol{U}_{\mathrm{SGS}} \tag{1}$$

where the overbar stands for the application of a LES filtering operator, and $\boldsymbol{U}_{\mathrm{SGS}}$ refers to the usual (unresolved) subgrid scales in the LES terminology.

In the following, it will then be chosen to work with the perturbation variables $\boldsymbol{U}'$ to compute turbulent fluctuations around the mean field $\langle \boldsymbol{U} \rangle$ computed using the RANS approach, with a similar degree of accuracy as that obtained with classical LES.

As a starting point for the derivation of a set of evolution equations for the fluctuating field $\boldsymbol{U}'$, let us first consider the following compact notations for the Navier–Stokes equations:

$$\frac{\partial \boldsymbol{U}}{\partial t} + \mathcal{N}(\boldsymbol{U}) = 0 \tag{2}$$

where $\mathcal{N}$ denotes the Navier–Stokes operator:

$$\mathcal{N}(\boldsymbol{U}) = \begin{pmatrix} \nabla \cdot (\rho \boldsymbol{u}) \\ \nabla \cdot (\rho \boldsymbol{u} \otimes \boldsymbol{u}) + \nabla p - \nabla \cdot \sigma \\ \nabla \cdot ((\rho E + p)\boldsymbol{u}) - \nabla \cdot (\sigma \cdot \boldsymbol{u}) + \nabla \cdot \boldsymbol{q} \end{pmatrix} \tag{3}$$

where p denotes the pressure, ρ is the density, $\boldsymbol{u} = (u, v, w)^T$ is the velocity vector, ρE is the total energy density, σ is the viscous stress tensor, and $\boldsymbol{q}$ is the heat flux vector. By subtracting the associated averaged and filtered NS equations and considering that the mean field $\langle \boldsymbol{U} \rangle$ is steady, the following set of the so-called nonlinear disturbance equations (NLDEs) is obtained (see [4,21–23] for details) for the perturbation variables $\boldsymbol{U}'$:

$$\frac{\partial \boldsymbol{U}'}{\partial t} + \mathcal{N}(\boldsymbol{U}' + \langle \boldsymbol{U} \rangle) = \mathcal{T}_L \tag{4}$$

where $\mathcal{T}_L$ denotes the usual subgrid terms that can be accounted for using any classical subgrid model. In this study, the selective mixed-scale model has been selected as the subgrid closure. This model was fully assessed in the works by Lenormand et al. [27,28] and is described in detail in the monograph by Sagaut [29].

At the boundaries of the LES region, the RANS solution is imposed as the mean field, whereas a nonreflecting characteristic approach is used for the turbulent fluctuations. Considering the moderate value of the Reynolds number, the flow is expected to remain laminar on the leading-edge surface of the slat. As a consequence, no turbulent fluctuations have been introduced in the boundary layers at the inflow of the LES region. Note that the generation of proper turbulent inflow conditions for aeroacoustic calculations generally leads to spurious noise and still remains an open issue. As will be discussed later in the paper, the fluctuations in the slat-cove shear layer are self-excited and self-sustaining and are not based on external disturbances. Finally, classical adiabatic nonslip boundary conditions are used at the walls, whereas periodicity conditions are used in the spanwise direction.

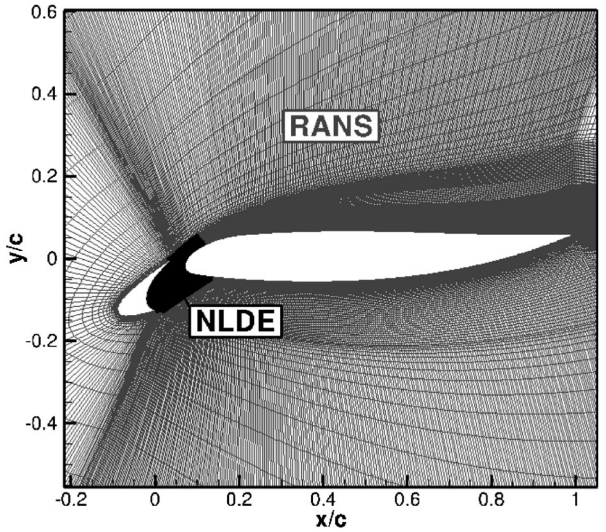

Fig. 13 Domain decomposition between the 3-D LES/NLDE region (plain black surface) and the 2-D RANS region (grey mesh).

B. Simulation Parameters and Numerical Method

Starting from the RANS grid topology used for the optimization step, a finer grid has been generated to perform the unsteady simulation. This grid is highly refined in the slat-cove region because it is aimed at resolving this area in the LES mode, as can be observed in Fig. 14 (see the discussion at the end of Sec. IV.C.1). The grid cell size used near the walls is 2×10^{-5} nondimensional units in the wall normal direction (i.e., 6×10^{-6} m), which ensures that the wall-normal grid resolution remains lower than one wall unit all along the

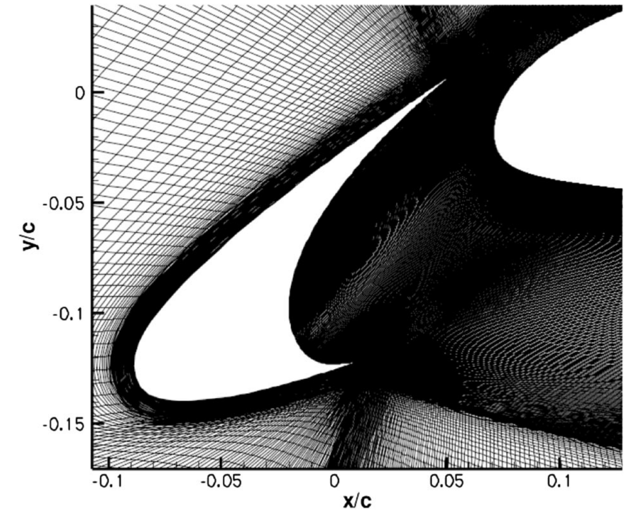

Fig. 14 Close-up view of the grid in the slat-cove area.

airfoil. This fine grid consists of 585,000 cells in the 2-D x-y plane, to be compared to the original grid used for the two-element airfoil RANS simulation of 126,000 cells. The grid in the slat-cove area (plain black surface in Fig. 13) has been duplicated in the spanwise direction using N_z discretization points. Note that, in this specific 2-D case, grid points match one-to-one in the x-y plane between the RANS and NLDE domains, but a no-match strategy can be adopted in the more general case to save grid points in the RANS areas.

Different spanwise extents have been considered: $L_z = c_s/4$, $L_z = c_s/2$, and $L_z = c_s$, where $c_s \simeq 0.13c \simeq 39$ mm is the chord of the slat. As detailed in Table 2, two different spanwise grid resolutions have also been investigated for the case $L_z = c_s/2$. The finest resulting three-dimensional (3-D) grid in the slat-cove area is composed of roughly 30 million points. For the coarsest spanwise grid resolution (used for simulations A, B1, and C), the ratio of the spanwise spacing to the spacing in the planar grid is between 2 and 3 in the main part of the slat cove. The twice-finer grid B2 therefore approaches isotropic spacing with a ratio between 1 and 1.5, which might be better for LES. The numerical scheme used to perform these unsteady computations is the modified AUSM+(P) scheme [30], which makes it possible to minimize the numerical dissipation by introducing a wiggle detector. Time integration uses a second-order implicit backward Euler scheme.

The resolution has been performed using the ONERA in-house research code FUNk, using 45 (case A) and 90 (cases B1, B2, and C) Intel Nehalem processors (2.8 GHz). Unsteady flow calculations have been conducted with a time step of 2×10^{-7} s. At each time step, the resolution involves a Newton resolution process for which eight inner subiterations are used. As will be detailed later on, only simulation C was considered for the unsteady analysis and therefore required a consequent physical integration time; starting from the steady RANS solution, this computation has been performed during a transient physical integration time of 54 ms (representing about 60 characteristic times of the main recirculation bubble in the slat cove). After this, statistics and unsteady data have been gathered over a physical time of 60 ms. The total cost of this simulation is approximately 26,000 CPU hours, for a total physical time of 114 ms.

Table 2 Characteristics of the computational domain (slat chord $c_s = 39$ mm

Simulation	Spanwise extent L_z	N_z	Δz	N_{xyz}
A	$c_s/4$	32	$\simeq 3 \times 10^{-4}$ m	$\simeq$7,586,000
B1	$c_s/2$	64	$\simeq 3 \times 10^{-4}$ m	$\simeq$15,172,000
B2	$c_s/2$	128	$\simeq 1.5 \times 10^{-4}$ m	$\simeq$30,345,000
C	c_s	128	$\simeq 3 \times 10^{-4}$ m	$\simeq$30,345,000

C. Main Flow Features and Statistical Analysis

1. Main Flow Features

Figure 15 shows instantaneous isosurfaces of the Q criterion, for the four different simulations. It must be noted that the level of resolved turbulence inside the slat cove is very high because a significant value of $Qc^2/U_\infty^2 = 10{,}000$ must be considered to isolate coherent structures in a visible manner. The general aspect of the flow appears to be similar for the four cases, although simulation B2 seems to exhibit finer resolved turbulent structures, due to the enhanced spanwise grid resolution. It can also be noted that large packets of vortices organizing themselves as streamwise-oriented vortices are observed at the trailing edge of the slat. However, despite the enhanced spanwise grid resolution used for simulation B2, the initial structure of the main shear layer is similar compared to simulation B1. For simulation A, one of these packets covers a spanwise extent, which appears to be of at least half of the total computed spanwise extent; therefore, in this case, the flow is likely to be affected by the spanwise periodicity condition.

As detailed in Figs. 16 and 17, several physical phenomena are observed.

1) A large recirculation bubble occurs in the slat and is surrounded by a large shear layer originating from the lower trailing edge.

2) A fast 2-D/3-D transition occurs in this shear layer, which finally impinges on the upper wall.

3) At the impingement location, large contrarotating streamwise-oriented vortices and hairpin vortical structures are visible.

4) Some of these structures are reinjected into the main recirculation bubble, whereas the others are strongly accelerated, convected downstream, and interact with the trailing edge.

5) An additional mixing layer is also visible at the trailing edge due to bluntness-induced vortex shedding.

Complex interactions between these different phenomena are also observed. As will be detailed later on in the paper, the impingement of the main shear layer on the upper surface of the slat is one of the most important phenomena occurring in the slat cove that leads to noise generation.

A good indicator of the adequacy of the grid to properly resolve the main shear-layer dynamics is based on the local ratio between the characteristic lengths of the shear layer and the local grid resolution in each flow direction (see the discussion in [23]). In the general case of a plane mixing layer between two parallel flows with respective velocities U_1 and U_2, the most-unstable wavelengths in the streamwise and spanwise directions are, respectively, $\lambda_x = 7\delta_\omega$ and $\lambda_z = 2/3\lambda_x = 14\delta_\omega/3$, where δ_ω is the local vorticity thickness. Its expression is

$$\delta_\omega = |U_1 - U_2| / \max(\mathrm{d}U/\mathrm{d}n) \tag{5}$$

where n denotes the shear-normal direction. Additionally, in the shear direction, the characteristic length is $\lambda_y = \delta_\omega$.

Following the trajectory of the main shear layer, the mean vorticity thickness has been estimated at several streamwise stations using relation (5). Its evolution as well as the corresponding local ratios between the characteristic wavelengths and the grid resolution are plotted in Fig. 18 for simulation C. From this figure, it appears that the local grid resolution used in the 2-D x-y plane is compatible with the numerical scheme, with at least 15 and up to 175 points per wavelength. In the early stages of the shear layer near the cusp, the grid resolution in the spanwise direction appears, however, a bit too coarse to fully account for 3-D effects, but the shear layer is expected to be essentially two-dimensional in this region. Note that simulation B2, using a twice-finer mesh in the spanwise direction, did not show any changes in the early stage dynamics of the shear layer.

2. Statistical Analysis

Figure 19 displays the mean spanwise vorticity component distribution and the mean flow streamlines in the slat-cove area for the various unsteady simulations, compared to the original RANS result. It is striking that all of the simulations lead to a modification of the main recirculation bubble aspect compared to the RANS

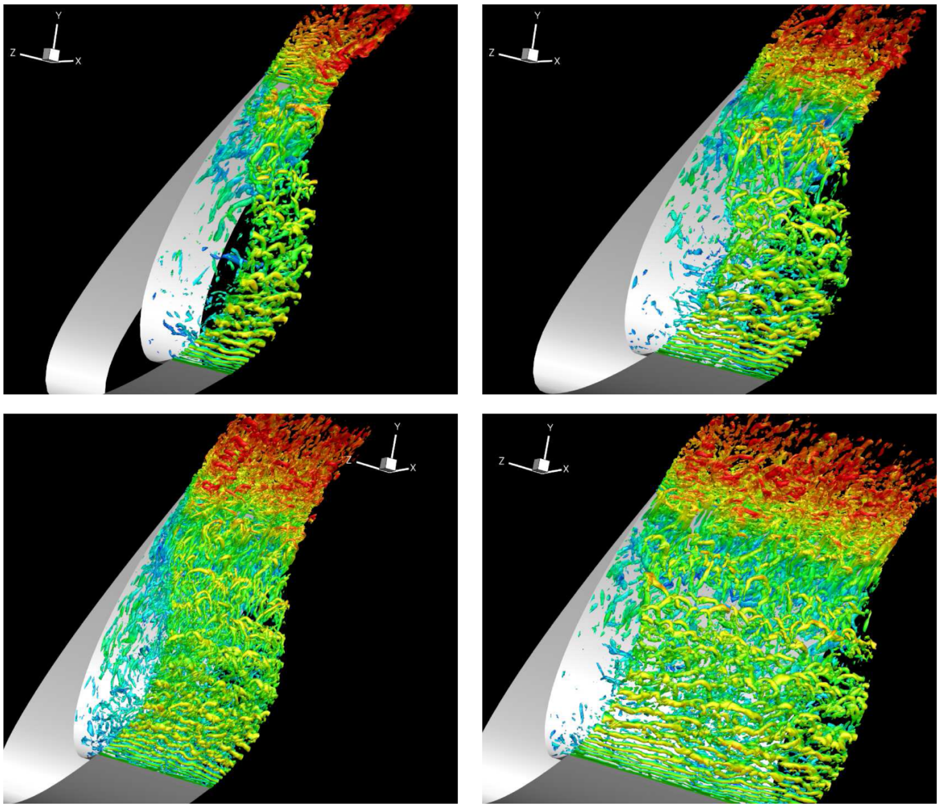

Fig. 15 Instantaneous iso-Q surfaces in the slat-cove region ($Q_{cz}/U_{z\infty} = 10{,}000$). Top: simulation A (left); simulation B1 (right). Bottom: simulation B2 (left); simulation C (right).

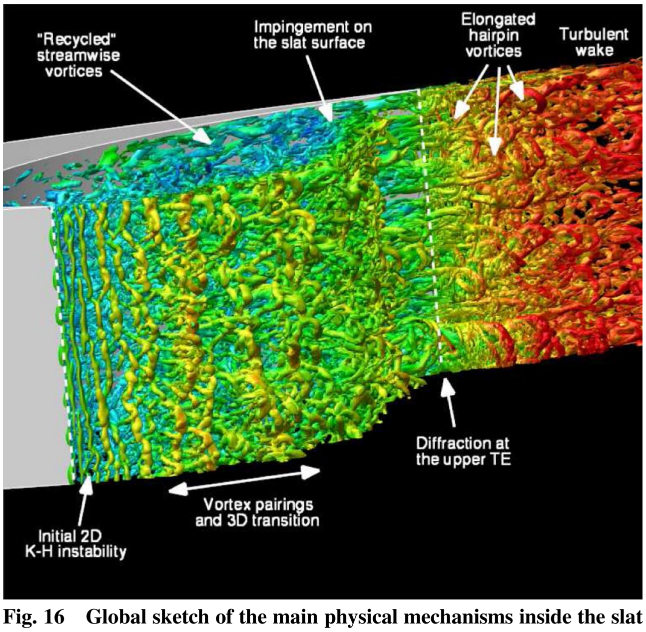

Fig. 16 Global sketch of the main physical mechanisms inside the slat cove. The main wing element has been removed to facilitate the visualization.

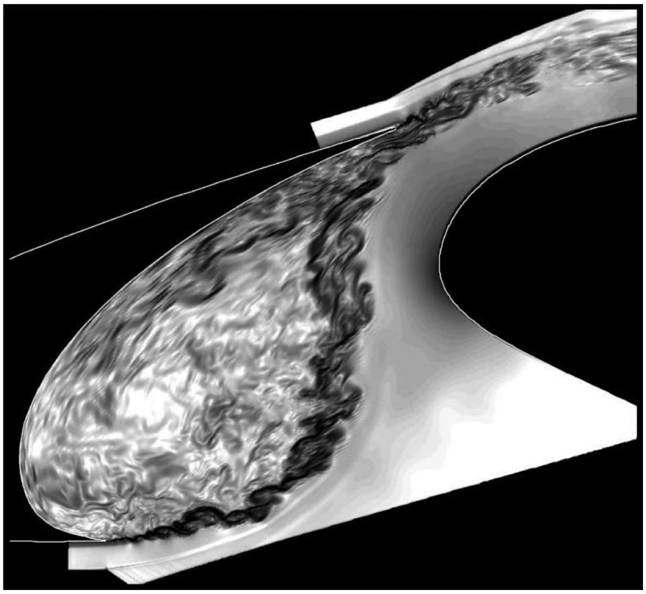

Fig. 17 Instantaneous Schlieren-like view (distribution of $|\nabla(\rho)|$ in a plane) in the slat-cove region.

simulation, which seems unable to correctly predict the development of the main shear layer. The spanwise vorticity magnitude in the main shear layer is dramatically increased in the unsteady simulations compared to the steady RANS result, with similar levels in all of the four zonal simulations that compare favorably with Jenkins et al. [15] particle image velocimetry (PIV) measurements under quite similar flow conditions and to existing numerical results [7,12–14]. It must be noted that the point where the main shear layer impinges the upper wall of the slat is shifted downstream in all of the turbulence-resolving simulations, to $x/c \simeq 0.0409$, compared to $x/c \simeq 0.0356$ for the RANS–SA computation. A similar trend can be observed in the numerical study by Deck [10], where steady RANS–SA computations seem to slightly underestimate the size of the separated region. It can be observed that the two simulations B1 and B2, corresponding to the same spanwise extent but with different spanwise grid resolutions, lead to a similar aspect of the mean flow. Simulation C, using the largest spanwise extent, also provides a very similar result. This is, however, not the case for the short-span simulation A, in which the vorticity seems to be enhanced at the center of the main recirculation bubble. This is a classical 2-D effect

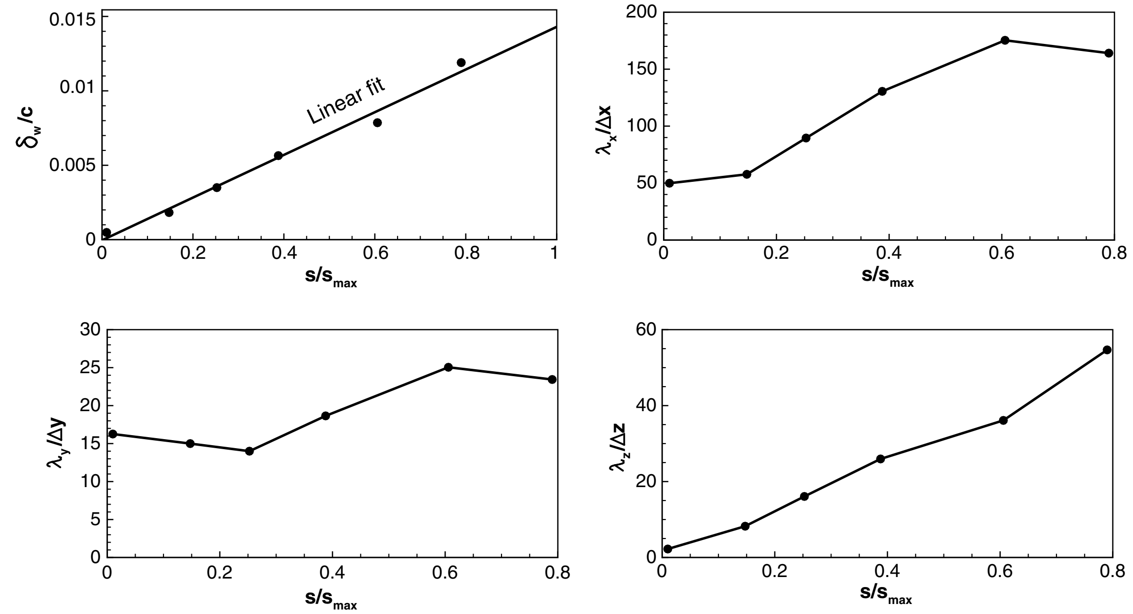

Fig. 18 Streamwise evolutions of characteristic length scales along the main shear layer for simulation C, as a function of the streamwise curvilinear coordinate *s*.

that indicates that the spanwise extent of the computational domain may be too short in this simulation.

The mean resolved turbulent kinetic energy (TKE) distributions obtained in each zonal computation are shown in Fig. 20. All simulations lead to significant levels of TKE along the main shear layer and to a region of high TKE levels where this shear layer impinges on the upper slat surface and interacts with the trailing edge. This region appears to be distributed over quite a wide area, due to the large amount of flow unsteadiness and shear-layer flapping around this location. Such a distribution is in good qualitative agreement with the experimental PIV [15] or LDA [16] visualizations and with the numerical results of Choudhari and Khorrami [12], Lockard and Choudhari [13,14], and Imamura et al. [7], who also observed similar TKE levels. It must be noted that the corresponding 2-D TKE levels (computed only from the x and y components of the velocity fluctuations) in the main shear layer are of the order of $0.02U_\infty^2$, which is in close agreement with the PIV measurements by Jenkins et al. [15] under similar flow conditions. Again, it can be observed that simulations B1 and B2 lead to quite similar distributions. It can also be observed that the large-span simulation C leads to higher TKE levels inside the main recirculation bubble, which may be due to a better representation of large-scale spanwise oscillations of the main vortex core.

Figure 21 shows the rms wall pressure coefficient distribution inside the slat cove obtained in the zonal simulations. These distributions are in good qualitative agreement with available numerical studies [12–14]; all of the simulations exhibit a strong peak of C_p' at $x/c \simeq 0.04$ that is clearly associated with the impingement of the main shear layer on the upper surface of the slat, as can be seen in Fig. 22. This phenomenon is therefore expected to be one of the main sources of sound in the slat-cove area. It can be noted that simulations B1 and B2 lead again to similar results, whereas simulation C leads to a higher peak level of C_p'.

To investigate the effect of the spanwise extent of the computational domain in more detail, the two-point spanwise correlation coefficient has been investigated. The two-point spanwise correlation coefficient of the shear-normal component of the velocity (similar trends are obtained for other flow quantities) computed in each simulation at several discrete points located along the main shear layer (points M_2, M_7, M_{12}, and M_{17}; see Fig. 23 for details) is plotted in Fig. 24. In regard to these curves, several comments can be made. Simulation A is clearly unable to reproduce a proper decorrelation along the span, due to a too-short spanwise extent; simulations B1 and B2 lead to similar results, therefore indicating that the spanwise grid resolution corresponding to simulations A, B1, and C should be sufficient; in these two simulations, it appears, however, that the spanwise extent of $c_s/2$ is a bit too short, or just what is needed, to allow a full spanwise decorrelation. Simulation C with $L_z = c_s$ seems more suitable to properly represent the spanwise integral lengths. This observation is in good agreement with the conclusions of Lockard and Choudhari [13] that a spanwise extent of about $0.8c_s$ is necessary to achieve a proper spanwise decorrelation of the flow. Based on these observations, the following developments will be focused on simulation C only.

3. *Comparison with Steady-State Experimental Results*

Figure 25 presents the mean pressure coefficient distributions obtained in the simulation, compared to the measurements. In this figure, the aforementioned NLDE mean flow correction can also be observed; the mean C_P distribution inside the slat cove is indeed modified for the unsteady simulation, compared to the steady RANS solution. From a more general point of view, there is still a mismatch between the measured and computed C_P distributions on the main wing element, due to a remaining difference in the effective angle of attack between the simulation and the experiment. This demonstrates that the freestream conditions employed in numerical simulations are difficult to match in open-jet wind tunnels.

The results of the simulation can also be compared to the hot-wire measurements.The following velocity norm has therefore been computed and averaged, in span and in time, during the simulation:

$$U_\perp = \sqrt{u^2 + v^2 + k^2 w^2} \tag{6}$$

where u, v, and w denote the velocity components in the streamwise x, vertical y, and spanwise z directions, respectively. Using this definition, $U_\perp$ corresponds to the effective velocity measured by the hot wire. The parameter k is dependent on the length-to-diameter ratio of the hot wire (see [31] for instance). In our study, $k = 0.1$ (numerical tests performed with $k = 0$ did, however, not show visible differences on the results). Note, however, that the rms fluctuation of $U_\perp$, computed according to relation (6) during the simulation, is actually very different from

$$\sqrt{u'^2_{\mathrm{RMS}} + v'^2_{\mathrm{RMS}} + k^2 w'^2_{\mathrm{RMS}}}$$

Figure 26 presents the two measurement rakes included in the NLDE region: rake "Slat Lower (SL)", which is located 1 mm

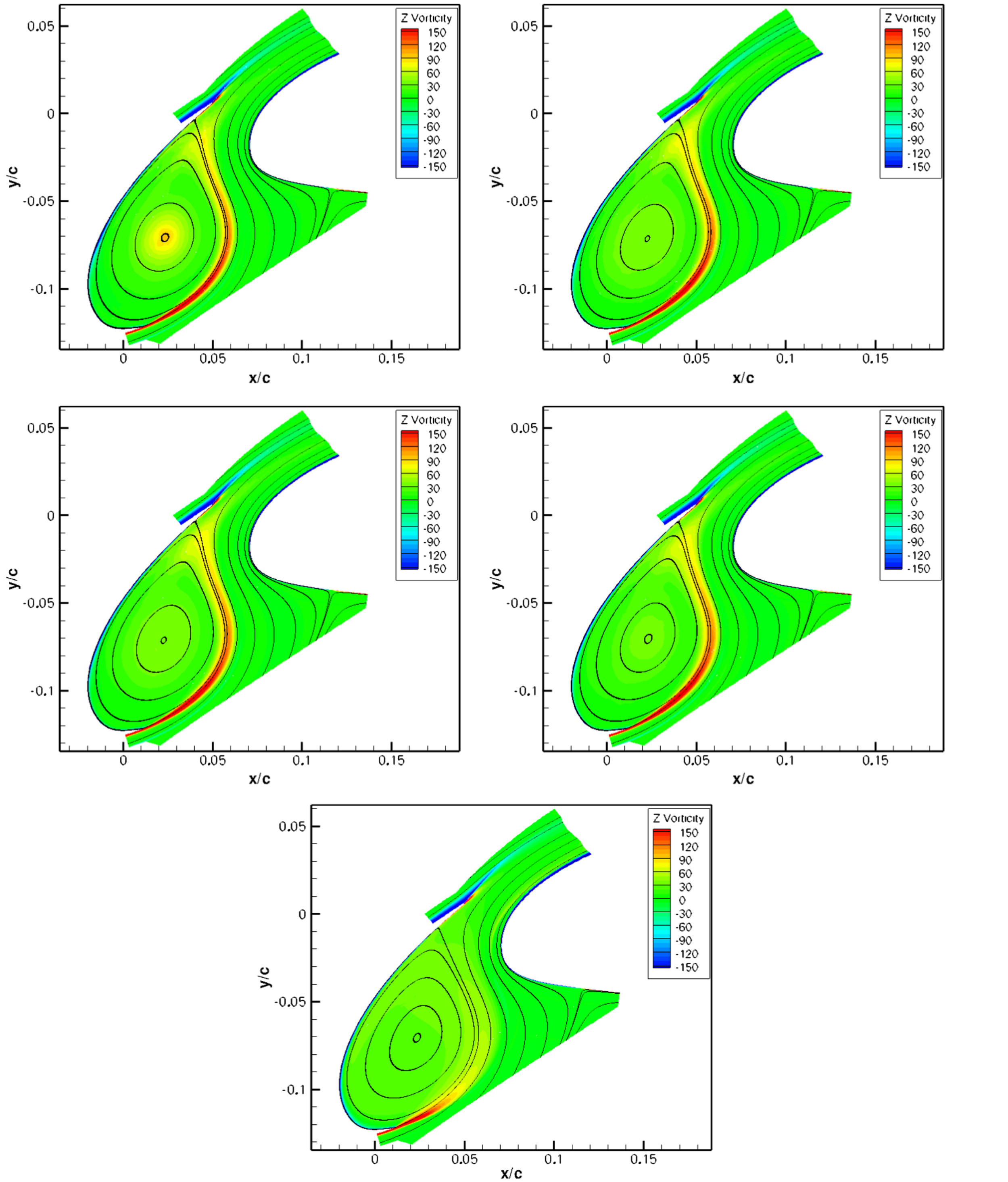

Fig. 19 Mean spanwise vorticity component distribution and mean flow streamlines in the slat cove. Top: simulation A (left); simulation B1 (right). Center: simulation B2 (left); simulation C (right); Bottom: RANS.

downstream of the cusp, and rake "Slat Upper (SU)", which is located 1 mm downstream of the trailing edge. Figure 27 displays the mean velocity and rms velocity fluctuation profiles for rake SL. The agreement between the simulation and the experiment is fair for the mean velocity, considering the remaining difference in the effective angle of attack. The agreement is quite good for the rms velocity fluctuations, especially considering that rake SL is located in a very sensitive area of the flow, highly receptive to external disturbances (freestream turbulence for instance); the global level of fluctuations inside the slat cove is well predicted, except very close to the cusp, where the peak value at $y/c \simeq -0.12$, due to the birth of fluctuations in the initial shear layer, is underestimated. Figure 28 presents the same kind of comparison for the upper rake SU. Again, a fair agreement with the hot-wire measurements is observed. The typical double-peak distribution of the rms velocity fluctuations is well recovered. The first peak around $y/c \simeq 0.004$ is slightly overestimated in the simulation but still in very reasonable agreement with the measurements. This indicates that the slat-cove turbulence passing through the gap is well predicted. The second peak at $y/c \simeq 0.008$ due to the development of instabilities in the wake of the trailing edge is of significantly higher amplitude in the simulation but may simply have been "missed" in the measurements due to an insufficient vertical resolution.

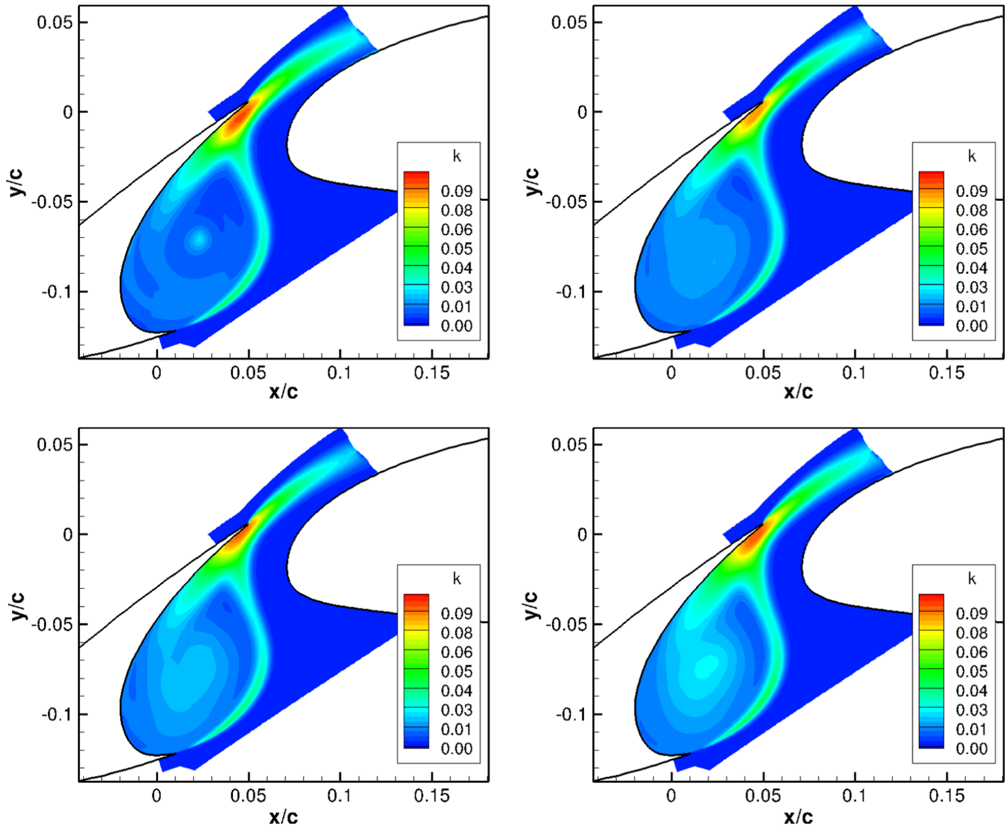

Fig. 20 Mean resolved turbulent kinetic energy distribution in the slat cove. Top: simulation A (left); simulation B1 (right). Bottom: simulation B2 (left); simulation C (right).

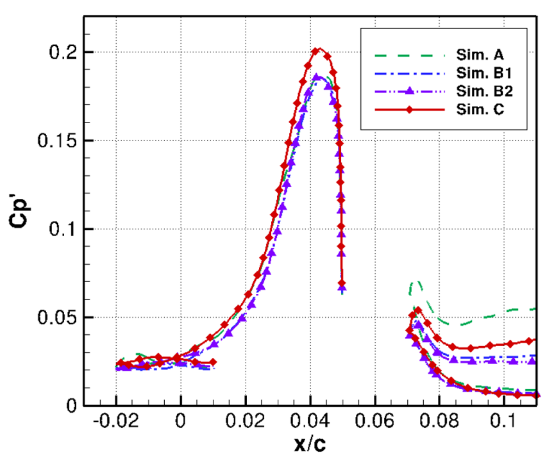

Fig. 21 RMS wall pressure coefficient distribution inside the slat cove.

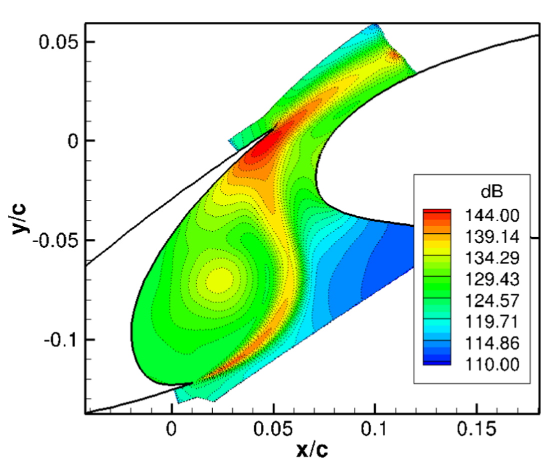

Fig. 22 RMS pressure distribution in the slat-cove region (simulation C).

D. Unsteady Flow Analysis

The following unsteady analysis has been performed for simulation C only, according to the conclusions of the previous section. As mentioned previously, unsteady data have been gathered after a transient time of 54 ms, during a physical time of 60 ms. These data have been used to compute velocity and pressure spectra for each extraction point, with a frequency resolution of 100 Hz. The convergence of the simulation can be observed by looking at Fig. 29, which shows the time history of the global lift coefficient.

Several numerical probes have been introduced in the computational domain, as depicted in Fig. 23. Each probe consists in practice of a rake of 128 points in the spanwise direction, allowing a spanwise averaging of the spectra to be performed. At each of these points, the

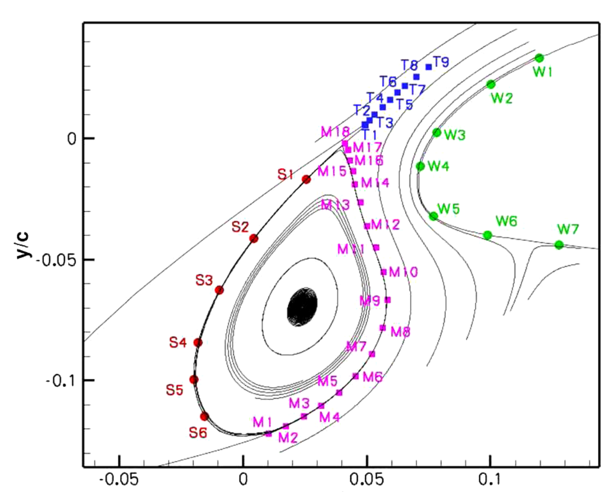

Fig. 23 Unsteady numerical probes locations in the slat cove, superimposed on mean flow streamlines.

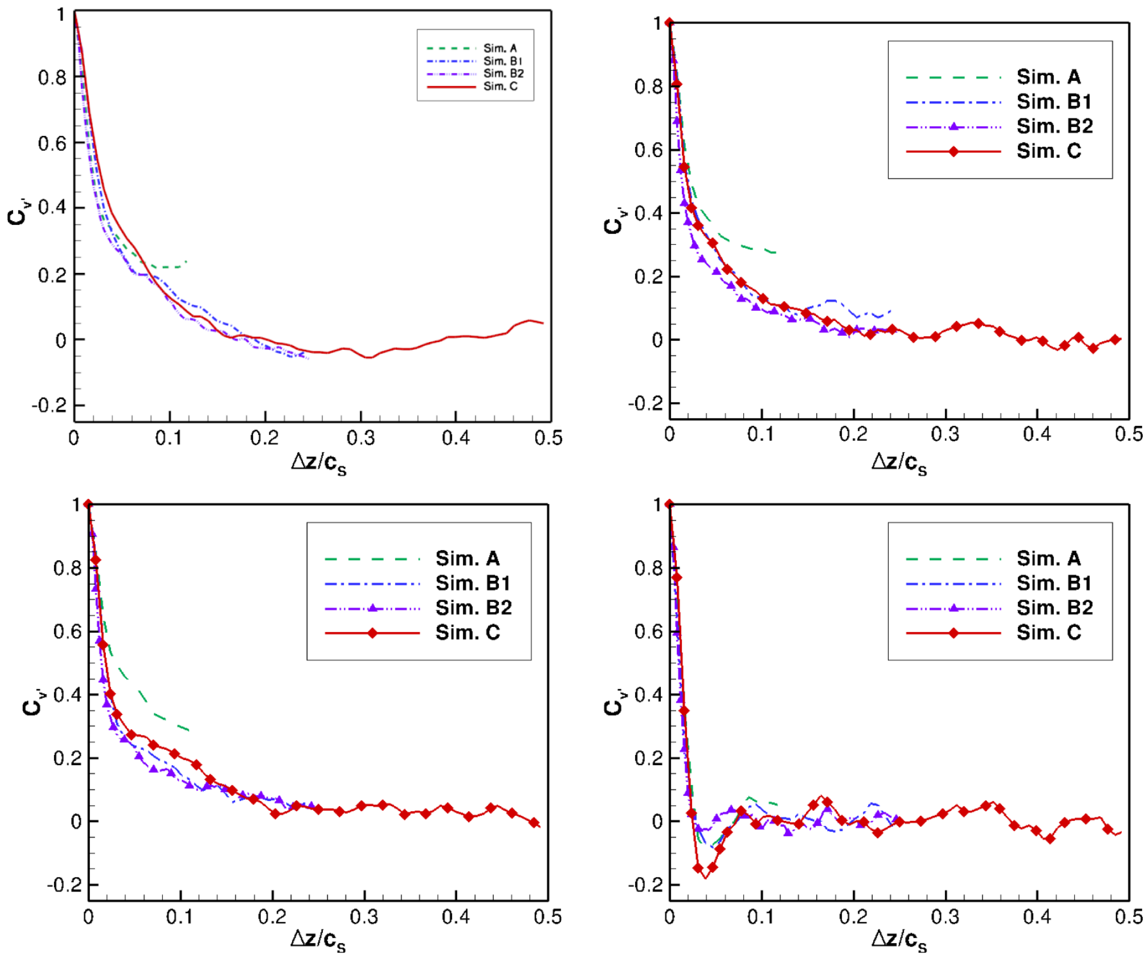

Fig. 24 Two-point spanwise correlation coefficient of velocity along the main shear layer. Top: probe M_2 (left); probe M_7 (right). Bottom: probe M_{12} (left); probe M_{17} (right).

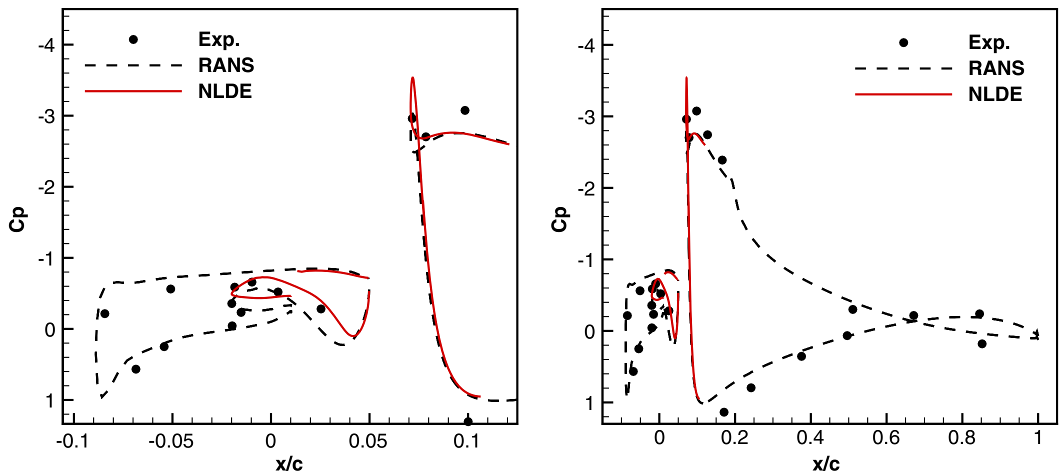

Fig. 25 Numerical (simulation C) and experimental steady-state pressure coefficient distributions of the optimized two-element airfoils. Left: slat region only; right: full airfoil.

unsteady field has been stored in time, with a sampling frequency of 1 MHz (i.e., one time step over five to avoid aliasing of the data).

1. Identification of Main Physical Features

Figure 30 shows the evolution of the spectral content of the flow along the mean shear-layer trajectory. It is interesting to note that a broadband hump around 25 kHz is present in all of the spectra at the beginning of the shear layer. This frequency has been identified as the main amplified frequency in the mixing layer occurring at the slat cusp, i.e., it is linked to the development of initial Kelvin–Helmholtz (K–H) instabilities, as observed in Fig. 17. Indeed, in the general case of a mixing layer between two parallel flows with respective velocities U_1 and U_2, this frequency can be estimated as $f_0 = \frac{1}{2}(U_1 + U_2)/(7\delta_0)$, where $\delta_0 = |U_1 - U_2|/\max(\mathrm{d}U/\mathrm{d}n)$ is the initial vorticity thickness (n denotes the shear-normal direction). The initial velocity profile and its associated normal derivative in this case are shown in Fig. 31, leading to $\delta_0 \simeq 2 \times 10^{-4}$ m and $f_0 \simeq 25.4$ kHz, which corresponds to the observed frequency. This broadband hump then shifts gradually toward lower frequencies when advancing along the shear layer, which is the signature of

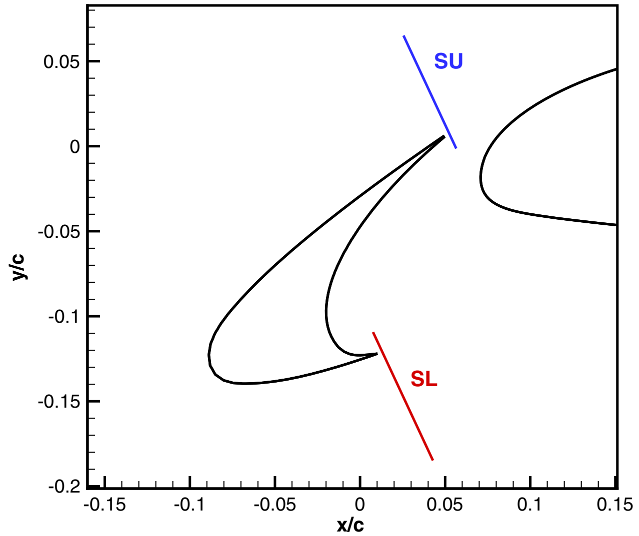

Fig. 26 Location of the hot-wire anemometry measurement rakes used for comparison.

vortex merging. Finally, at the end of the shear layer, an inertial range is visible in the spectra for the three components of velocity, as in fully developed turbulent mixing layers.

Figure 32 shows the streamwise evolution of the spectral content of the flow in the wake downstream of the trailing edge. All of the spectra are characterized by a broadband hump around 40 kHz, which is due to the vortex shedding from the blunt trailing edge interacting with the upstream turbulence coming from the cove. Similar spectra have been observed by Khorrami et al. [1]. By focusing on the velocity spectra, it is striking that the turbulence downstream of the cove is far from being isotropic, as can also be observed in instant views (see Fig. 16) where large streamwise-oriented and hairpin vortices are visible.

Figure 33 shows the wall pressure power spectral density (PSD) computed on the slat surface, at points S_1–S_6 (see Fig. 23). At point S_1, which is the closest one from the impingement location of the main shear layer, strong levels of wall-pressure fluctuations are observed, over a wide range of frequencies, due to the high turbulence intensity of the flow in that area. As far as the global turbulence level decreases by moving away from the impingement point, the global level of the pressure spectra also decreases significantly. It can be seen that several peaks appear at some discrete frequencies (~1800, 2500, 3500, 4350, and 5200 Hz, with an accuracy of ± 50 Hz), which are a priori not linked to any of the aerodynamic physical events listed previously. As can be seen in Fig. 9, strong peaks at these frequencies also emerge from the broadband content as tonal components in the far-field acoustic spectra. Section V will be devoted to a possible physical interpretation of these tones. By approaching the slat cusp (points S_4, S_5, and S_6), the broadband hump around 25 kHz is recovered in the pressure spectra. As mentioned previously, this

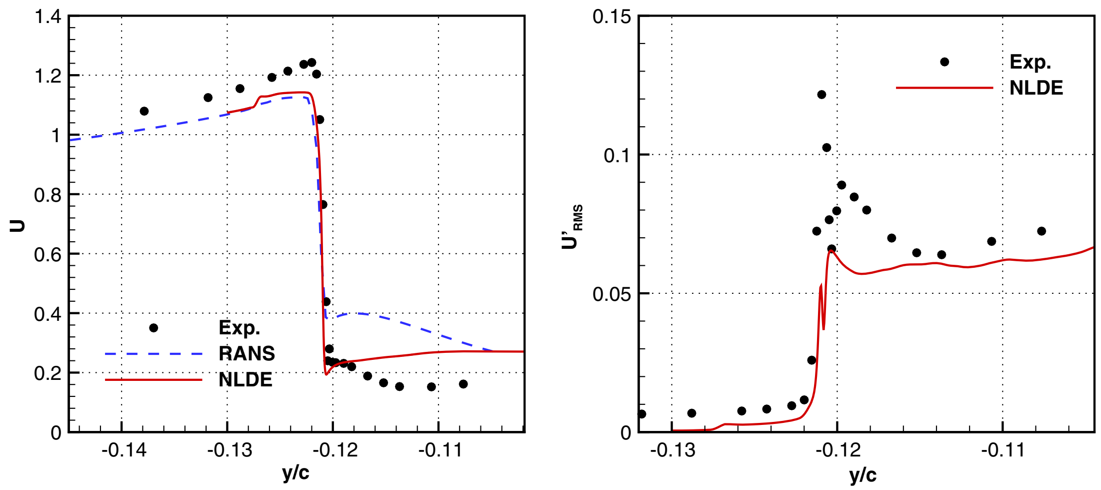

Fig. 27 Mean velocity (left) and rms velocity fluctuations (right) from simulation C, compared to the hot-wire anemometry measurements along rake SL (see Fig. 26). Velocity is normalized by the freestream velocity.

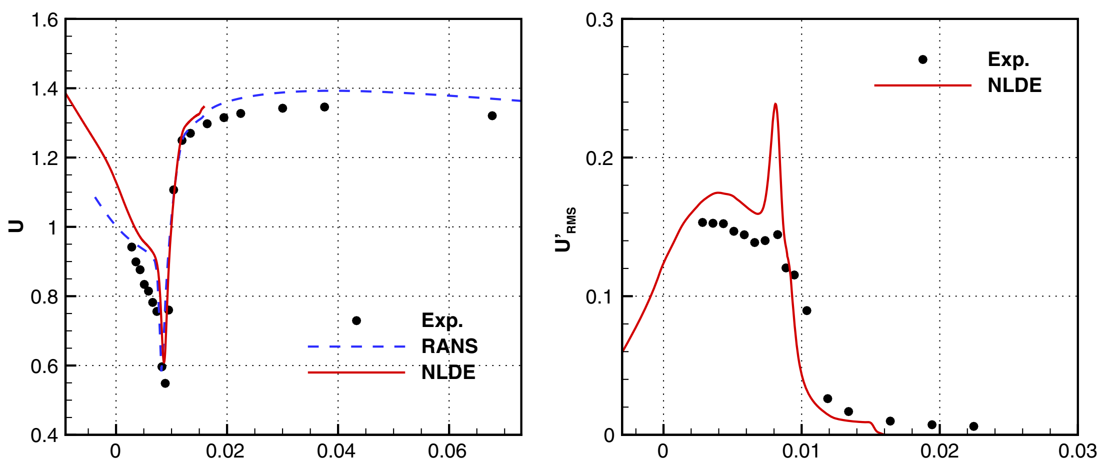

Fig. 28 Mean velocity (left) and rms velocity fluctuations (right) from simulation C, compared to the hot-wire anemometry measurements along rake SU (see Fig. 26). Velocity is normalized by the freestream velocity.

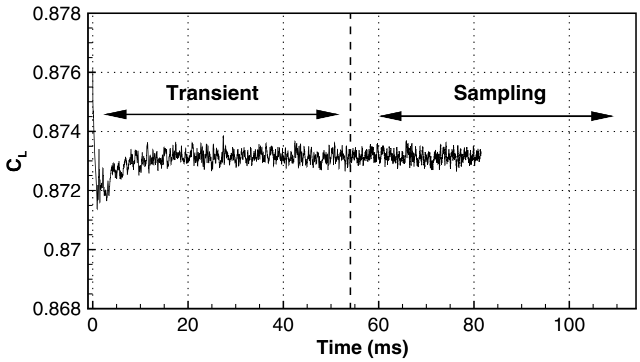

Fig. 29 Time history of the global lift coefficient (simulation C).

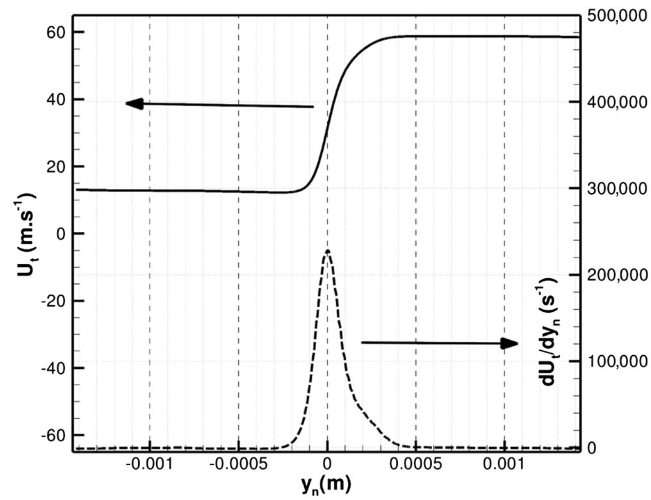

Fig. 31 Tangential velocity profile and associated shear-normal derivative used for the estimation of the vorticity thickness at the beginning of the main shear layer.

hump in the spectra appears to be linked to K–H instabilities developing in the main shear layer.

Figure 34 shows the wall pressure PSD computed at the surface of the main wing element, in the leading-edge region (i.e., at points W_1–W_7; see Fig. 23). Probes W_1 and W_2 located downstream of the gap reveal broadband spectra where no specific peaks are observed. This is certainly due to the presence of the highly turbulent flow coming from the slat cove. At the other points, several peaks are visible at the same discrete frequencies as those observed at the slat surface and in the acoustic field. These peaks are mostly visible for points W_6 and W_7 located in a flow region where the pressure field is not contaminated by turbulent structures. The broadband hump around 25 kHz is still visible there, indicating that the shear layer itself is correlated with the overall noise. Regularly spaced smaller peaks are also visible at high frequencies, which may be the signature of a temporal modulation of the signal with an associated modulation frequency of the order of 9 kHz. Although such a modulation may be attributed to wave reflections inside the slat cove, this phenomenon remains quite unclear up to now.

Finally, it is worth noting that the pressure spectra exhibit a general f^{-3} dependency (except in fully turbulent regions), consistent with previous works [17,18].

2. *Comparison with Experimental Results*

The computed wall pressure spectra have been compared with the experimental results. The following experimental spectra have been obtained using a theoretical expression [32] of the frequency-

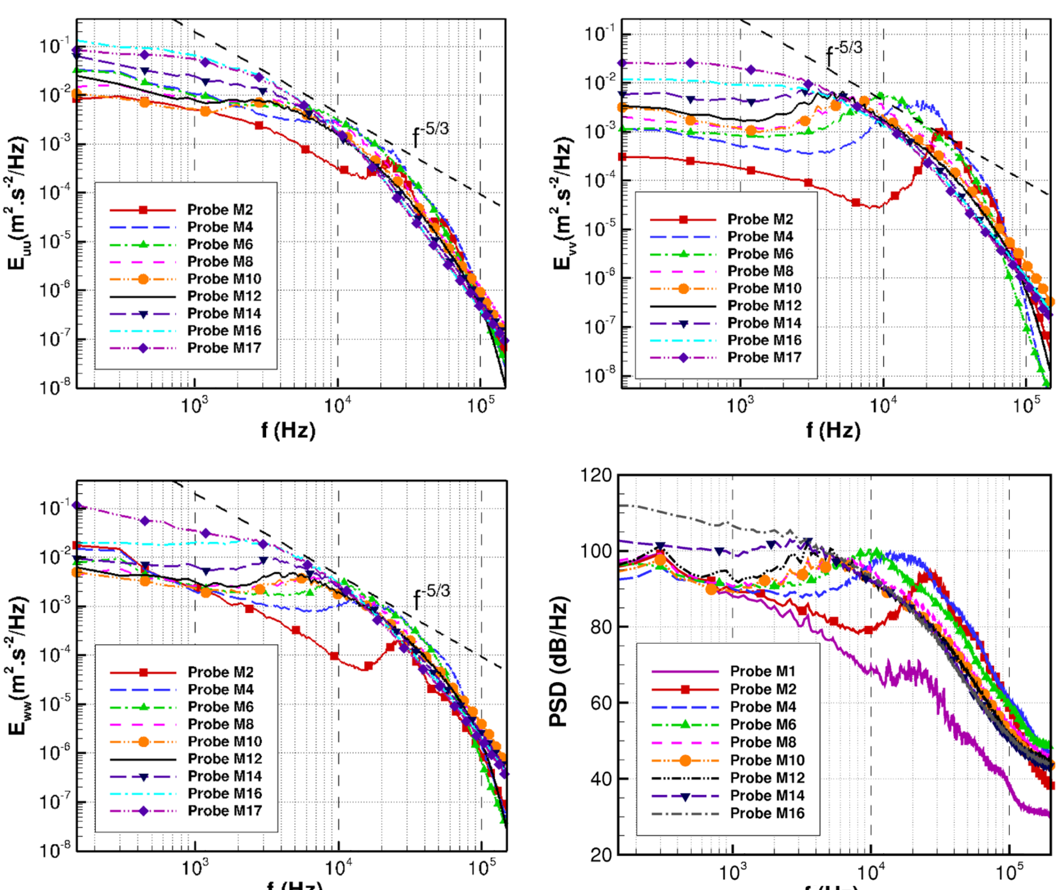

Fig. 30 Velocity and pressure spectra along the main shear layer (probes M_2–M_{17}). Top: streamwise (left) and vertical (right) components of velocity. Bottom: spanwise component of velocity (left) and pressure (right).

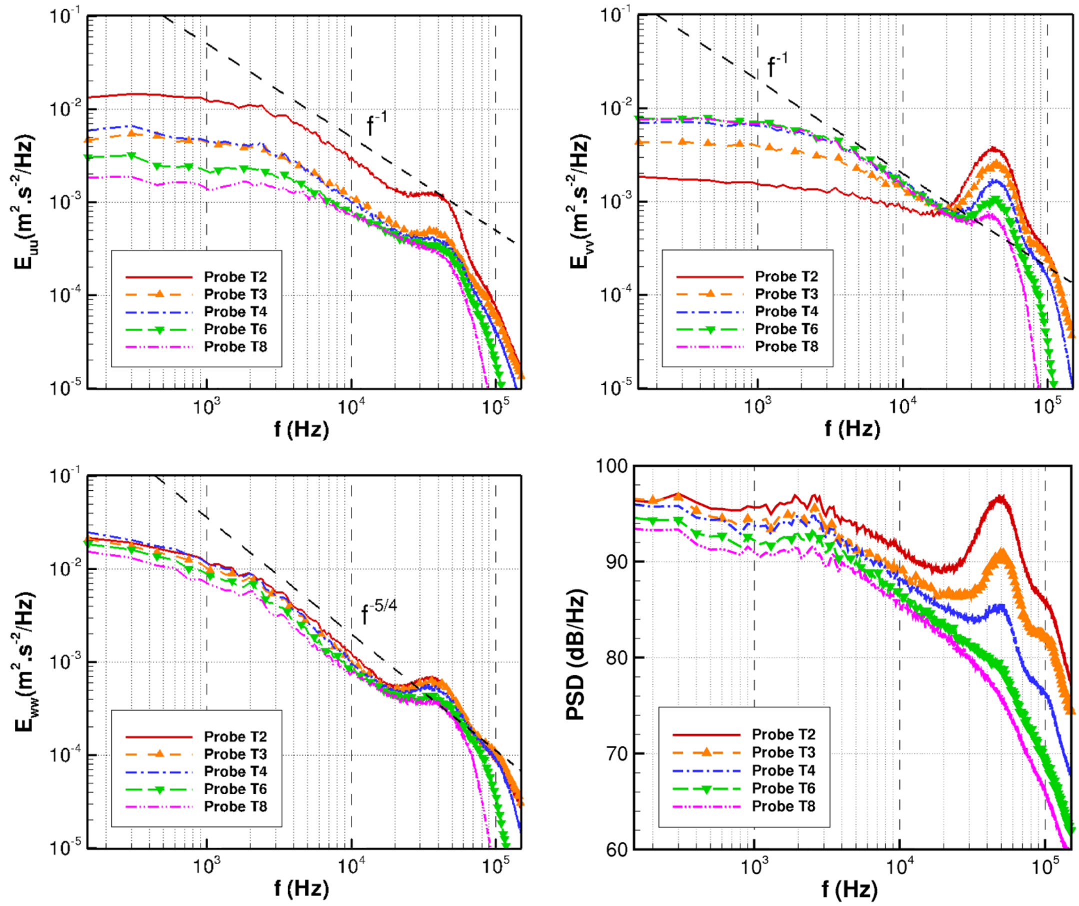

Fig. 32 Velocity and pressure spectra along the wake of the TE (probes T_2–T_8). Top: streamwise (left) and vertical (right) components of velocity. Bottom: spanwise component of velocity (left) and pressure (right).

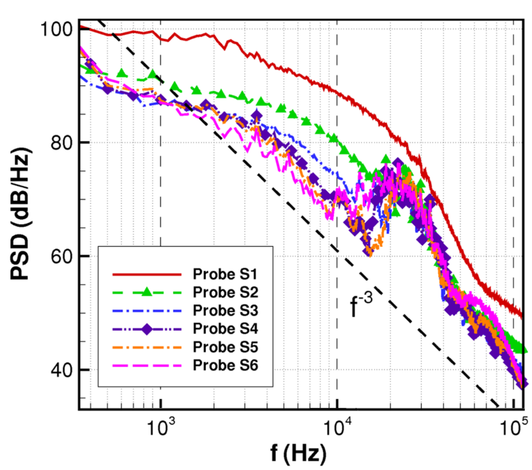

Fig. 33 Computed wall pressure spectra at several points along the slat surface. See Fig. 23 for detailed points locations.

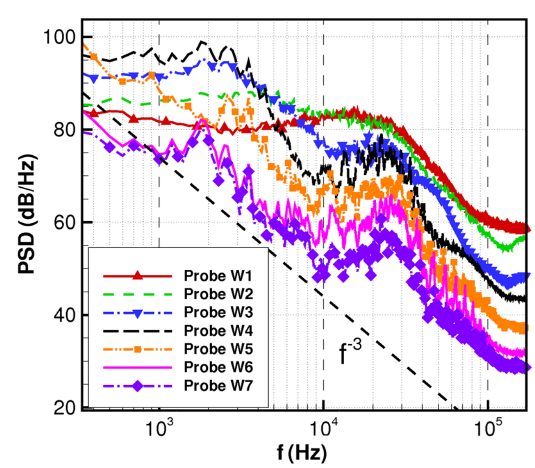

Fig. 34 Computed wall pressure spectra at several points located in the leading-edge region of the main wing element. See Fig. 23 for detailed points locations.

response function for each probe, although a more rigorous treatment should involve an experimental calibration, which is not easy to perform because of difficult access.

A comparison of the computed wall pressure power spectral densities on the slat surface with experimental results is presented in Fig. 35. For points S1 and S2, which are the closest ones from the impingement point of the main shear layer on the slat surface, it can be seen that the global magnitude of the spectra obtained in the simulation is higher than in the experiment, which may reveal a higher degree of turbulence. For the other points considered, S4 to S6, the global broadband trend of the spectra is well recovered with a very satisfactory prediction of the global level. It must be noted that the broadband frequency hump around 25 kHz attributed to the initial 2-D structures of the main shear layer is also present in the measurements. For all of the considered points, the tonal peaks present in the measurements are present in the simulation, but with a significantly less pronounced magnitude: the spectra obtained in the simulation exhibit a more broadband content, especially close to the impingement point. Similar trends in the pressure spectra are observed in the experimental results of Imamura et al. [17]. The exact reason for that difference between experimental and computational results remains unclear up to now. It could be related to the difficulties of accurately reproducing by the code the acoustic feedback responsible for the amplification of the tones. Another possible issue may be due to a too-fast three-dimensional breakup of the slat-cusp

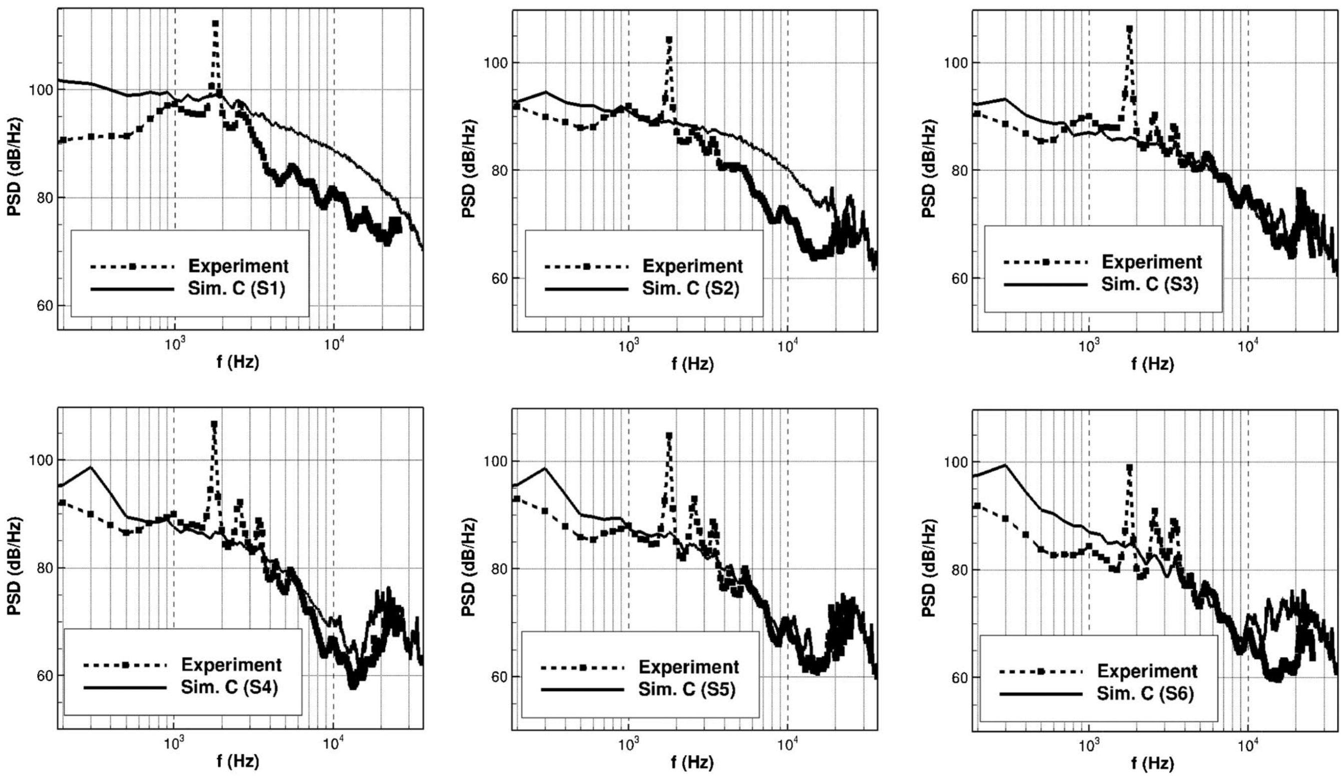

Fig. 35 Comparison between computed wall pressure spectra and experimental measurements along the slat surface. See Fig. 23 for detailed locations of probes S_1–S_6.

shear layer in the simulations, leading to less coherent large-scale vortices and a weaker source. Indeed, too-dissipative simulations or purely 2-D simulations are generally observed to increase the tonal peaks artificially, due to a higher spanwise coherence of the vortices. Note also, as already stated in Sec. III, that a small change in the effective angle of attack of the airfoil may result in significant differences in the amplitude of the tonal peaks. Because it is very difficult in practice to exactly match the flow conditions between the freestream calculations and open-jet experiments, some differences may be present in the tonal peaks amplitudes.

V. Physical Interpretation of Discrete Tones

As detailed in the previous sections, both the acoustic and aerodynamic fields are characterized by the presence of tonal components in the pressure spectra. Such tones are observed both in the experimental and numerical results, at midrange frequencies that could not be related directly to any specific flow features. It must be noted that the presence of tonal components in slat-noise measurements is not a new observation and that several experimental works reported in literature exhibit the presence of such a feature in the acoustic spectra. However, the exact reason for their existence remains quite unclear up to now, although two possible explanations are generally considered. The first one postulates these tones as being due to laminar effects (i.e., to a feedback loop between the acoustic waves and Tollmien–Schlichting waves generated in the slat boundary layers). Such a coupling has mainly been investigated both experimentally and numerically for a simple airfoil [33–38] and remains an open topic. Under this assumption, the tonal components are therefore considered as being a direct consequence of low-Reynolds-number effects and are therefore expected to disappear at full scale (i.e., when the boundary layers at the slat surface become naturally turbulent). The possible occurrence of a coupling between acoustic waves and boundary-layer instability waves on the suction surface of a slat was only studied recently by Makiya et al. [39], who observed such a coupling in low-Reynolds-number experiments (chord-based Reynolds numbers only up to 5.9×10^5) of the flow past a two-element airfoil. In this work, additional experimental tests have been performed by including a transition strip at the upper surface of the slat to artificially trigger the transition of the boundary layer. It was observed that, in this case, tonal noise components were still present in the acoustic spectra. Such an observation was also made by Pott-Polenske et al. [19] and Kolb et al. [18], who did not obtain any significant effect of the tripping devices on tonal frequency removal, therefore arguing for a quite stable underlying physical mechanism. In practice, tone removal seems to be only obtained when using quite thick serration strips (with a width of the order of the boundary-layer thickness itself), which may also affect the mean flow. In their experimental tests, Imamura et al. [17] also observed the occurrence of multiple tonal peaks in the acoustic spectra. The authors also indicate that using tripping devices on the lower slat surface did not work sufficiently to remove the tonal components. Therefore, it seems that forcing turbulent transition of the boundary layers is not sufficient to remove tonal components and that an additional quite stable physical mechanism is involved in the generation of multiple tonal peaks. Finally, it must also be noted that the reduced computational domain selected for our RANS/LES computations clearly does not make it possible to resolve any receptivity mechanism of the slat boundary layers, which are almost not included in the region computed by LES. Because our unsteady computations also exhibit the presence of discrete tonal peaks in the pressure spectra, it therefore seems that such a receptivity mechanism can be reasonably discarded.

One of the other possible scenarios relies on the existence of a feedback loop between the sound waves generated by the impingement of the main shear layer on the slat surface and the mixing layer originating from the slat cusp, as is the case for cavity flows. Such a scenario has been proposed by Roger and Pérennès [40], who observed experimentally that the slat cove and the flap cove of a 2-D high-lift airfoil generate tones in the same way as rectangular cavities under a grazing flow. In their experimental study, Imamura et al. [17] succeeded in removing the tonal components by using a slat-cove filler device. As indicated by these authors, the use of such a device makes it possible to suppress the main shear layer and its associated feedback loop, which appears as a convincing indication that the tonal peaks are strongly linked to the presence of the main shear layer. In their study, Kolb et al. [18] applied Rossiter's semi-

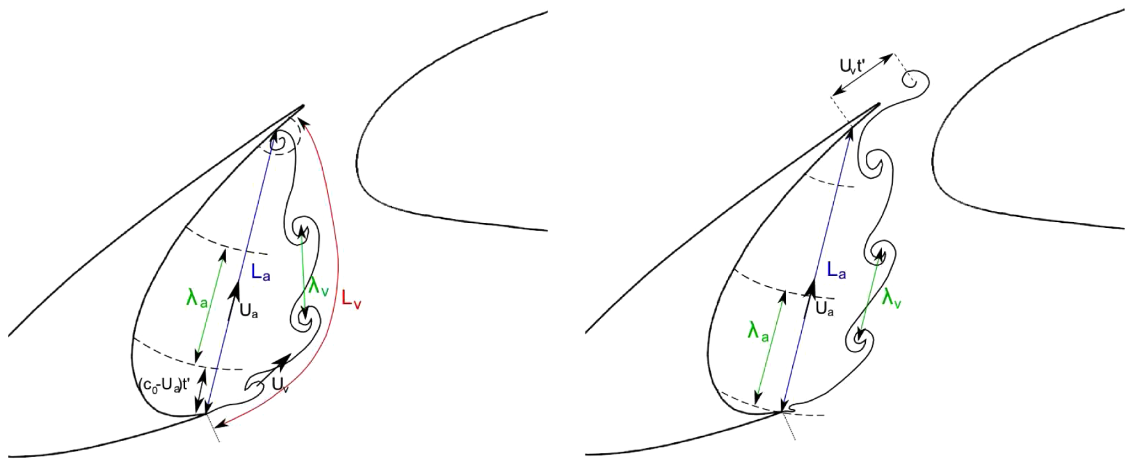

Fig. 36 Schematic representation of the aeroacoustic feedback loop inside the slat cove. Left: time t_0; Right: time $t_0 + t'$.

empirical formula quite successfully to analytically recover the discrete frequencies observed in their experiments. However, directly applying Rossiter's formula (originally developed for rectangular cavities [41]) to the flow inside the slat cove seems a bit questionable. Moreover, as indicated by the previous authors, this formula only depends on the freestream velocity and does not include any influence of the angle of attack. This parameter was observed in practice to exhibit a significant influence on the tonal frequencies. Such a dependency might be explained by the modification of the aspect of the main vortex core when varying the angle of attack, which results in a modification of the physical properties of the main shear layer and of the location of its impingement point on the surface. In the following, an improved formula inspired on Rossiter's original formula is proposed to predict the discrete frequencies originating from the slat cove.

A. Theoretical Derivation of the Tonal Frequencies

For the following developments, we will consider the simple scenario depicted by Fig. 36.

1) A given number n_v of vortices originating from the slat cusp are convected along the main shear layer surrounding the main vortex core inside the slat cove, at a mean convection velocity U_v. The distance between two vortices is denoted by λ_v.

2) One of these vortices finally impinges the surface of the slat and generates an acoustic wave (see Fig. 36, left).

3) The acoustic waves, of wavelength λ_a, are propagated through the slat cove. Introducing the projection of the mean flow velocity U_a inside the slat cove along the acoustic path (straight line between the impingement point and the slat cusp), these waves propagate at a speed of $(c_0 - U_a)$, where c_0 is the speed of sound.

4) One of these waves finally reaches the cusp, which leads to the generation of a new vortex in the main shear layer (see Fig. 36, right).

Let us now consider an instantaneous snapshot of the flow at a given time $t = t_0$, when a vortex impinges the trailing edge and generates a new acoustic wave, as depicted in the left part of Fig. 36. Further introduce t' the time needed for an acoustic wave to reach the cusp and generate a new vortex. At this new time $t = t_0 + t'$, the former vortex has traveled a downstream distance of $U_v t'$. Introducing the two lengths L_a and L_v as depicted in Fig. 36, we can write the following simple phase relations:

$$L_a = n_a \lambda_a + (c_0 - U_a)t' \tag{7}$$

$$n_v \lambda_v = L_v + U_v t' \tag{8}$$

where n_a is the number of acoustic fronts observed inside the slat cove at $t = t_0$. From these two relations, we get the equality

$$\frac{L_a - n_a \lambda_a}{c_0 - U_a} = \frac{n_v \lambda_v - L_v}{U_v} \tag{9}$$

Introducing the integer value $n = n_a + n_v$ and the frequency associated to the feedback loop

$$f_n = \frac{c_0 - U_a}{\lambda_a} = \frac{U_v}{\lambda_v}$$

we get

$$\frac{L_a U_v + L_v(c_0 - U_a)}{U_v(c_0 - U_a)} = \frac{n}{f_n} \Rightarrow f_n = n \frac{U_v(c_0 - U_a)}{L_a U_v + L_v(c_0 - U_a)}$$

Finally, introducing $\alpha_l = L_v/L_a$ the ratio of the shear-layer length to the acoustic path and the nondimensional velocities $\kappa_v = U_v/U_\infty$ and $\kappa_a = U_a/U_\infty$, the final formula holds:

$$f_n = n \frac{U_\infty}{L_a} \cdot \frac{1}{\frac{1}{1/\mathcal{M} - \kappa_a} + \frac{\alpha_l}{\kappa_v}} \tag{10}$$

where $\mathcal{M}$ is the freestream Mach number.

It has been observed on the basis of several 2-D RANS calculations that the mean flow velocity U_a along the acoustic path remains negligible over a wide range of angles of attack and freestream velocities. Therefore, for the following analysis, the parameter κ_a will be set to zero in Eq. (10), leading to the following simplified model:

$$f_n = n \frac{U_\infty}{L_a} \cdot \frac{1}{\mathcal{M} + \frac{\alpha_l}{\kappa_v}} \tag{11}$$

Several comments can be made about this relation.

1) The two parameters α_l and κ_v are dependent upon the flow itself. They are besides expected to be significantly affected by the angle of attack, the freestream velocity or the airfoil geometry. Such a dependency and the additional dependency on the freestream Mach number can be the reason why the tonal frequencies are usually not observed to follow a simple Strouhal scaling.

2) No empirical parameter is used in the model as for instance the β parameter present in Rossiter's original formula. This parameter is usually interpreted as a temporal delay between the impingement of one vortex on a solid surface and the generation of an acoustic wave, but the physical reason for such a behavior remains quite unclear.

3) An accurate application of this model requires the estimation of the three parameters L_a, α_l (or L_v), and κ_v. This point will be addressed in the next section.

B. Numerical Estimation of the Model Parameters

As seen in the previous section, relation (11) makes it possible to estimate analytically the tone frequencies. However, for that purpose, several flow-dependent parameters need being estimated, namely L_a, κ_v, and α_l.

The two first parameters depend only on the mean flow properties, more precisely on the aspect of the main vortex core and on the location of the impingement point of the main shear layer. Therefore, they can be estimated very simply by mean flow streamlines visualizations. For the specific case computed in this study, the analysis of the mean field given by NLDE yields $L_a = 0.1217c$, where $c = 0.3$ m is the retracted chord of the airfoil, and $\alpha_l = 1.1724$. It is to be noted that the steady RANS result already provides values of these quantities in a reasonable agreement with these assessments (i.e., $L_a = 0.1172c$ and $\alpha_l = 1.204$).

The estimation of the mean convection velocity U_v in the mean shear layer is somewhat more tricky. The most rigorous way to value this quantity relies on the introduction of the two-time/two-point correlation coefficient of two scalar quantities f and g:

$$\mathcal{C}(\xi,\tau) = \frac{\langle f(s,t)\cdot g(s+\xi,t+\tau)\rangle - \langle f(s,t)\rangle\langle g(s+\xi,t+\tau)\rangle}{\sqrt{\langle f(s,t)^2\rangle - \langle f(s,t)\rangle^2}\sqrt{\langle g(s,t)^2\rangle - \langle g(s,t)\rangle^2}} \tag{12}$$

where s denotes the curvilinear coordinate along the mean shear-layer trajectory, and the brackets denote a temporal and spanwise averaging operator. More precisely, we will consider the correlation coefficient based on the instantaneous pressure fluctuation p' at several points M_j located along the main shear-layer trajectory (points M_3 to M_{15} in Fig. 23). For each point M_j, the correlation coefficient is estimated for its five closest neighbors M_i, $i = j-2, \ldots, j+2$ as

$$\mathcal{C}(M_i,\tau) = \frac{\langle p'(M_j,t)\cdot p'(M_i,t+\tau)\rangle}{\langle p'(M_j,t)^2\rangle}, \quad \text{for } i = j-2,\ldots,j+2 \tag{13}$$

As an example, the corresponding pressure correlation coefficients evolutions for one selected point (M_8) are displayed in Fig. 37. For each physical point, the temporal shift τ corresponding to the maximum peak value of the correlation coefficient is considered, together with the corresponding spatial distance from the reference point M_j. These two quantities are plotted for point M_8 in Fig. 38, making it finally possible to estimate the local convection velocity. The obtained value at point M_8 is $U_v = 39.4\ \mathrm{m\cdot s^{-1}}$. The process has been repeated for several other points located along the mean shear layer, leading to a mean convection velocity of $U_v \simeq 40.3\ \mathrm{m\cdot s^{-1}}$ (i.e., $\kappa_v = 0.79$).

Relation (11) will therefore be applied using the following set of parameters:

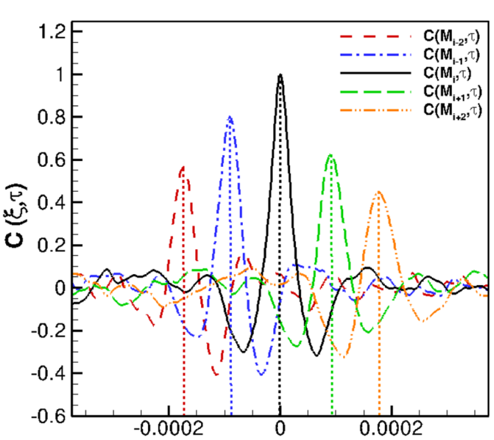

Fig. 37 Two-point/two-time pressure correlation coefficient at point M8 of the main shear layer.

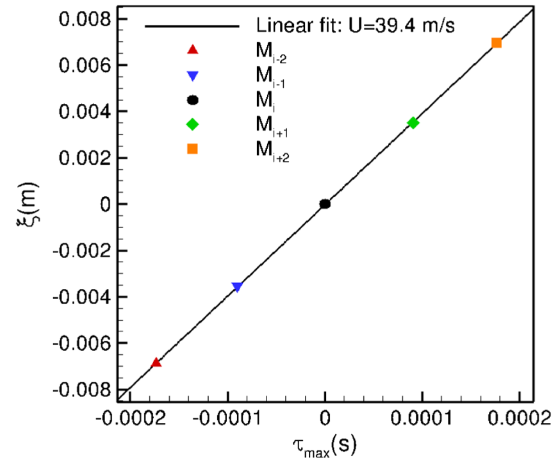

Fig. 38 Numerical estimation of the convection velocity in the main shear layer, using the peak locations of the two-point/two-time pressure correlation coefficient from Fig. 37.

$$L_a = 0.1217c, \quad \alpha_l = 1.1724, \quad \kappa_v = 0.79 \tag{14}$$

It should, however, be noted that using the unsteady results to estimate the model parameters reduces considerably the applicability field of such a relation. However, as it is the case for L_a and α_l, it appears that a reasonable estimation of the mean convection velocity in the mean shear layer can be obtained using only the steady RANS result. Figure 39 shows the evolution of the velocity magnitude along a mean flow streamline following the mean shear layer, for both the RANS and NLDE simulations. From this plot, it appears quite clear that the mean convection velocity can be approximated by the mean plateau value, providing an estimate of $\kappa_v = 0.77$ using the RANS result only, which is very close to the value of 0.79 obtained using the two-point/two-time correlation function. This last value also corresponds to the mean plateau value given by the averaged NLDE result.

C. Analytical Estimation of the Tonal Noise Frequencies

This section introduces the application of relation (11) to the prediction of the tonal frequencies for the present experimental setup, over a significant range of freestream velocities between 30 and 70 $\mathrm{m\cdot s^{-1}}$. Although the model parameters have only been estimated for the case corresponding to $U_\infty = 51\ \mathrm{m\cdot s^{-1}}$, it was observed on the basis of several steady RANS computations that these quantities do not change significantly when varying the freestream velocity. Therefore, the set of parameters given in Eq. (14) has been selected for the whole range of freestream velocities under consideration.

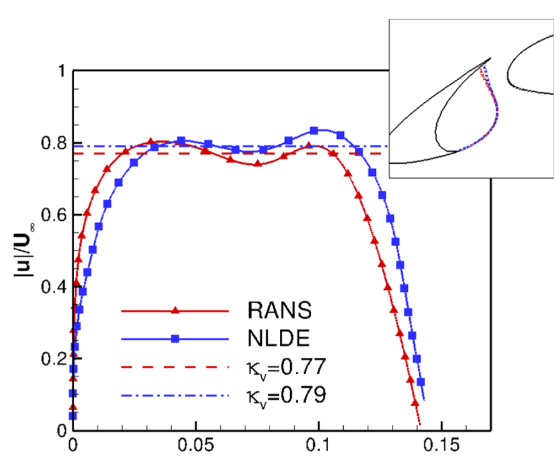

Fig. 39 Velocity magnitude evolution along a mean flow streamline following the mean shear layer. Comparison between the 2-D RANS and the averaged NLDE results.

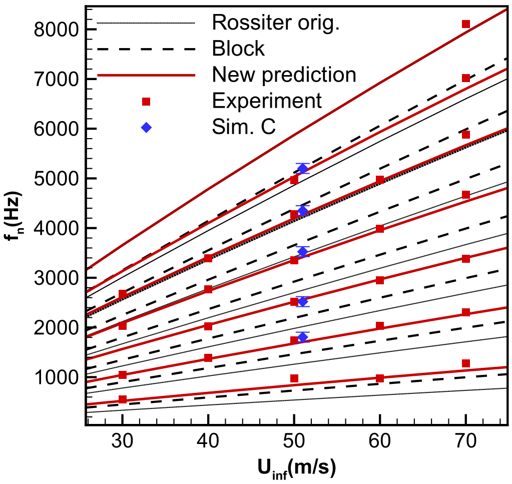

Fig. 40 Predicted and observed tonal frequencies as a function of the freestream velocity.

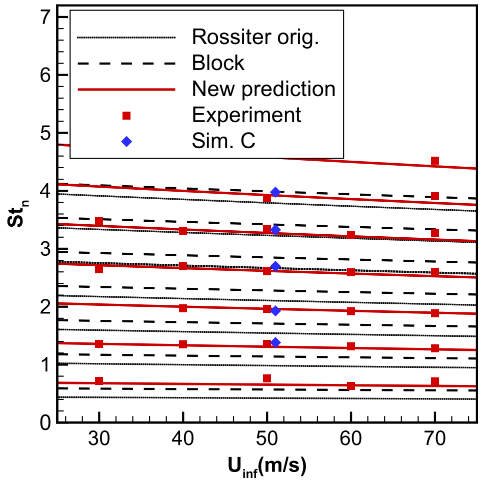

Fig. 41 Same as Fig. 40, in Strouhal scaling.

The frequencies obtained using the theoretical relationship are plotted in Figs. 40 and 41, in Strouhal scaling (using the freestream velocity U_∞ and the slat chord c_s as reference velocity and length). For each case, the results are compared to the far-field measurements (square symbols, see Fig. 9) and to unsteady NLDE results (diamond symbols). A comparison is also made with Rossiter's original formula [41]:

$$f_n = (n - \beta)\frac{U_\infty}{L_a} \cdot \frac{1}{\mathcal{M} + (1/\kappa)} \tag{15}$$

where the usual values $\beta = 0.25$ and $\kappa = 0.57$ have been considered.

Another relationship for cavity mode prediction is that proposed by Block [42], which introduces the length-to-depth ratio L_a/D to distinguish between shallow and deep cavities. Introducing the cavity depth D, its expression is

$$f_n = n\frac{U_\infty}{L_a} \cdot \frac{1}{(1/\kappa) + \mathcal{M}(1 + 0.514/(L_a/D))^{-1}} \tag{16}$$

This formula was recently shown to yield very good predictions for the tonal peak frequencies in the slat cove of a three-element airfoil by Deck and Laraufie [8]. The predictions from this model are therefore also included for comparison in Figs. 40 and 41 (D is estimated as the average normal distance between the shear layer and the slat surface, as performed in [8]).

For the entire range of velocities under consideration, it appears that Rossiter's original formula fails to accurately predict the tonal peak frequencies. Block's formula slightly improves the prediction compared to Rossiter's formula but still does not fit the measured and simulated frequencies. This model was, however, observed to yield very reliable predictions in [8] and would certainly require some tuning of the parameters to be more general. On the other hand, the proposed new relation [Eq. (11)] is observed to provide quite reliable estimates of the tonal frequencies for the entire range of velocities under consideration. This satisfying result and the theoretical developments performed to derive this relation therefore support the fact that the feedback loop depicted in Fig. 36 seems to be the main physical mechanism involved in the occurrence of tonal components.

VI. Conclusions

Experimental slat-noise investigations are usually quite difficult to perform. The main difficulty in open-jet wind tunnels, well suited for acoustic measurements, is directly linked to the high-lift property of the airfoil, which introduces a significant deviation of the main jet. To address this point, the first part of this study was therefore devoted to the design of a new two-element airfoil configuration, devoted to slat-noise analysis. This configuration 1) presents a flow in the slat-cove area that is representative of the flow in a realistic three-element configuration, and 2) significantly minimizes the global flow deviation and global lift force, which is mandatory for open-jet wind-tunnel tests. This configuration has been investigated experimentally in the open-jet anechoic wind-tunnel at the Centre Acoustique of the École Centrale de Lyon.

In a second step, several zonal Reynolds-averaged Navier–Stokes /large-eddy simulation simulations of the flow inside the slat cove of this two-element wing profile have been conducted, using different spanwise resolutions and spanwise extents of the computational domain. The unsteady flow in the slat-cove area exhibits rich physical characteristics. The computations have made it possible to identify the main noise sources, the most important one being due to the impingement of the main shear layer on the slat pressure side surface, close to the trailing edge. Secondary noise sources, such as the self-noise of the main shear layer due to Kelvin–Helmholtz instabilities, have also been identified using spectral analysis. A comparison of the wall-pressure spectra obtained in the simulation against experimental results has been carried out. The pressure spectra are characterized by tonal peaks emerging from a broadband content; these tonal components have been identified as being due to a feedback loop between the main shear layer and acoustic waves generated by the impingement of this layer on the slat surface, in a similar way as in cavity flows. A theoretical model to predict the tonal frequencies has been proposed and validated in the last part of the study.

Future works will focus on the coupling of the unsteady computational fluid dynamics calculation with an external acoustic solver based on integral methods. This coupling will then make it possible to obtain far-field unsteady pressure signals and perform an additional assessment of the calculations against the measurements. Additional simulations may also be necessary to account for the installation effects (nozzle, jet deviation) present in the open-jet facility. Such a computation seems necessary to ensure that the experiments and the simulations correspond to exactly the same physical conditions.

Acknowledgments

Part of this work was financed by the European Union project VALIANT, grant agreement ACP8-GA-2009-233680. The authors are very grateful to M. Roger for his help and fruitful discussions and to I. Le Griffon for providing the experimental far-field pressure spectra. S. Deck, L. Larchevêque, and I. Mary are also gratefully acknowledged for stimulating technical discussions.

References

[1] Khorrami, M. R., Berkman, M. E., and Choudhari, M., "Unsteady Flow Computations of a Slat with a Blunt Trailing Edge," *AIAA Journal*, Vol. 53, No. 12, 2000, pp. 2050–2058. doi:10.2514/2.892

[2] König, D., Koh, S. R., Meinke, M., and Schröder, W., "Two-Step Simulation of Slat Noise," *Computers and Fluids*, Vol. 39, No. 3, 2010, pp. 512–524.
doi:10.1016/j.compfluid.2009.10.004

[3] Zhong, B., Scheurich, F., Titarev, V., and Drikakis, D., "Turbulent Flow Simulations Around a Multi-Element Airfoil Using URANS, DES and ILES Approaches," *19th AIAA Computational Fluid Dynamics Conference*, AIAA Paper 2009-3799, 2009.

[4] Terracol, M., Manoha, E., Herrero, C., Labourasse, E., Redonnet, S., and Sagaut, P., "Hybrid Methods for Airframe Noise Numerical Prediction," *Theoretical and Computational Fluid Dynamics*, Vol. 19, No. 3, 2005, pp. 197–227.
doi:10.1007/s00162-005-0165-5

[5] Terracol, M., Labourasse, E., Manoha, E., and Sagaut, P., "Simulation of the 3D Unsteady Flow in a Slat Cove for Noise Prediction," *9th AIAA/CEAS Aeroacoustics Conference and Exhibit*, AIAA Paper 2003-3110, 2003.

[6] Terracol, M., and Deck, S., "Numerical Investigation of the Flow Around a Three-Element High-Lift Airfoil Using Two Zonal Hybrid RANS/LES Methods: ZDES and NLDE," *Progress in Hybrid RANS–LES Modelling*, Vol. 117, Notes on Numerical Fluid Mechanics and Multidisciplinary Design, Springer, Berlin, 2012, pp. 345–355.

[7] Imamura, T., Enomoto, S., Yokokawa, Y., and Yamamoto, K., "Three-Dimensional Unsteady Flow Computations Around a Conventional Slat of High-Lift Devices," *AIAA Journal*, Vol. 46, No. 5, 2008, pp. 1045–1053.
doi:10.2514/1.25660

[8] Deck, S., and Laraufie, R., "Numerical Investigation of the Flow Dynamics Past a Three-Element Aerofoil," *Journal of Fluid Mechanics*, Vol. 732, 2013, pp. 401–444.
doi:10.1017/jfm.2013.363

[9] Knacke, T., and Thiele, F., "Numerical Analysis of Slat Noise Generation," *19th AIAA/CEAS Aeroacoustics Conference*, AIAA Paper 2013-2162, 2013.

[10] Deck, S., "Zonal Detached-Eddy Simulation of the Flow Around a High-Lift Configuration," *AIAA Journal*, Vol. 43, No. 12, 2005, pp. 2372–2384.
doi:10.2514/1.16810

[11] Knacke, T., and Thiele, F., "Time-Resolved 3D Simulation of an Aircraft Wing with Deployed High-Lift System," *Proceedings of the Turbulence and Interactions TI2009 Conference*, Springer–Verlag, Berlin, 2010, pp. 223–230.
doi:10.1007/978-3-642-14139-3

[12] Choudhari, M., and Khorrami, M. R., "Effect of Three-Dimensional Shear-Layer Structures on Slat Cove Unsteadiness," *AIAA Journal*, Vol. 45, No. 9, 2007, pp. 2174–2186.
doi:10.2514/1.24812

[13] Lockard, D. P., and Choudhari, M., "Noise Radiation from a Leading-Edge Slat," *15th AIAA/CEAS Aeroacoustics Conference*, AIAA Paper 2009-3101, May 2009.

[14] Lockard, D. P., and Choudhari, M., "The Effect of Cross Flow on Slat Noise," *16th AIAA/CEAS Aeroacoustics Conference*, AIAA Paper 2010-3835, 2010.

[15] Jenkins, L. N., Khorrami, M. R., and Choudhari, M., "Characterization of Unsteady Flow Structures Near Leading-Edge Slat: Part 1. PIV Measurements," *10th AIAA/CEAS Aeroacoustics Conference*, AIAA Paper 2004-2801, 2004.

[16] Takeda, K., Ashcroft, G. B., Zhang, X., and Nelson, P. A., "Unsteady Aerodynamics of Slat Cove Flow in a High-Lift Device Configuration," *39th Aerospace Sciences Meeting and Exhibit*, AIAA Paper 2001-0706, 2001.

[17] Imamura, T., Ura, H., Yokokawa, Y., and Yamamoto, K., "A Far-Field Noise and Near-Field Unsteadiness of a Simplified High-Lift-Configuration Model (Slat)," *47th AIAA Science Meeting*, AIAA Paper 2009-1239, 2009.

[18] Kolb, A., Faulhaber, P., Dobrietz, R., and Grünewald, M., "Aeroacoustic Wind Tunnel Measurements on a 2D High-Lift Configuration," *13th AIAA/CEAS Aeroacoustics Conference*, AIAA Paper 2007-3447, 2007.

[19] Pott-Pollenske, M., Alvarez-Gonzalez, J., and Dobrzynski, W., "Effect of Slat Gap on Farfield Radiated Noise and Correlation with Local Flow Characteristics," *9th AIAA/CEAS Aeroacoustics Conference*, AIAA Paper 2003-3228, 2003.

[20] Dobrzynski, W., and Pott-Pollenske, M., "Slat Noise Sources Studies for Farfield Noise Prediction," *7th AIAA/CEAS Aeroacoustics Conference*, AIAA Paper 2001-2158, 2001.

[21] Labourasse, E., and Sagaut, P., "Reconstruction of Turbulent Fluctuations Using a Hybrid RANS/LES Approach," *Journal of Computational Physics*, Vol. 182, No. 1, 2002, pp. 301–336.
doi:10.1006/jcph.2002.7169

[22] Terracol, M., "A Zonal RANS/LES Approach for Noise Sources Prediction," *Flow, Turbulence and Combustion Journal*, Vol. 77, Nos. 1–4, 2006, pp. 161–184.
doi:10.1007/s10494-006-9042-6

[23] Sagaut, P., Deck, S., and Terracol, M., "Multiscale and Multiresolution Approaches in Turbulence," *LES, DES and Hybrid RANS/LES Methods: Applications and Guidelines*, 2nd ed., Imperial College Press, London, 2013, pp. 310–313.

[24] Wild, J., Pott Pollenske, M., and Nagel, B., "An Integrated Design Approach for Low Noise Exposing High-Lift Devices," *3rd AIAA Flow Control Conference*, AIAA Paper 2006-2843, 2006.

[25] Montigny Rannou, F., and Jacquotte, O. P., "MESH3D: Un Outil Pour la Construction de Maillages Tridimensionnels (in French)," *Proceedings of the 29th Applied Aerodynamics Symposium*, AAAF, 1992.

[26] Manoha, E., and Pott-Polenske, M., "LEISA2: An Experimental Database for the Validation of Numerical Predictions of Slat Unsteady Flow and Noise," *21st AIAA/CEAS Aeroacoustics Conference*, AIAA Paper 2015-3137, 2015.

[27] Lenormand, E., Sagaut, P., and Ta Phuoc, L., "Large-Eddy Simulation of Compressible Channel Flow at Moderate Reynolds number," *International Journal of Numerical Methods in Fluids*, Vol. 32, No. 4, 2000, pp. 369–406.
doi:10.1002/(ISSN)1097-0363

[28] Lenormand, E., Sagaut, P., Ta Phuoc, L., and Comte, P., "Subgrid-Scale Models for Large-Eddy Simulation of Compressible Wall Bounded Flows," *AIAA Journal*, Vol. 53, No. 8, 2000, pp. 1340–1350.
doi:10.2514/2.1133

[29] Sagaut, P., "Large-Eddy Simulation for Incompressible Flows," *Scientific Computation*, 3rd ed., Springer–Verlag, Berlin, 2005, p. 130.

[30] Mary, I., and Sagaut, P., "Large Eddy Simulation of Flow Around an Airfoil Near Stall," *AIAA Journal*, Vol. 40, No. 6, 2002, pp. 1139–1145.
doi:10.2514/2.1763

[31] Champagne, F. H., Sleicher, C. A., and Wehrmann, O. H., "Turbulence Measurements with Inclined Hot-Wires Part 1. Heat Transfer Experiments with Inclined Hot-Wire," *Journal of Fluid Mechanics*, Vol. 28, No. 1, 1967, pp. 153–175.
doi:10.1017/S002211206700196X

[32] Pérennès, S., "Caractérisation des Sources de Bruit Aérodynamique à Basses Fréquences de Dispositifs Hypersustentateurs (in French)," Ph.D. Thesis, École Centrale de Lyon, Lyon, France, 1999.

[33] Paterson, R. W., Vogt, P. G., and Fink, M. R., "Vortex Noise of Isolated Airfoils," *Society of Naval Architects and Marine Engineers, and U.S. Navy, Advanced Marine Vehicles Meeting*, AIAA Paper 1972-0656, 1972.

[34] Tam, C. K. W., "Discrete Tones of Isolated Airfoils," *Journal of the Acoustical Society of America*, Vol. 55, No. 6, 1974, pp. 1173–1177.
doi:10.1121/1.1914682

[35] Arbey, H., and Bataille, J., "Noise Generated by Airfoil Profiles Placed in a Uniform Laminar Flow," *Journal of Fluid Mechanics*, Vol. 134, No. 1, 1983, pp. 33–47.
doi:10.1017/S0022112083003201

[36] Lowson, M. V., Fiddes, S. P., and Nash, E. C., "Laminar Boundary Layer Aero-Acoustic Instabilities," *32nd Aerospace Sciences Meeting and Exhibit*, AIAA Paper 1994-0358, 1994.

[37] Lowson, M. V., McAlpine, A., and Nash, E. C., "The Generation of Boundary Layer Instability Noise on Aerofoils," *36th AIAA Aerospace Sciences Meeting and Exhibit*, AIAA Paper 1998-0627, 1998.

[38] Desquesnes, G., Terracol, M., and Sagaut, P., "Numerical Investigation of the Tone Noise Mechanism over Laminar Airfoils," *Journal of Fluid Mechanics*, Vol. 591, Nov. 2007, pp. 155–182.
doi:10.1017/S0022112007007896

[39] Makiya, S., Inasawa, A., and Asai, M., "Vortex Shedding and Noise Radiation from a Slat Trailing Edge," *AIAA Journal*, Vol. 48, No. 2, 2010, pp. 502–509.
doi:10.2514/1.45777

[40] Roger, M., and Pérennès, S., "Low-Frequency Noise Sources in Two-Dimensional High-Lift Devices," *5th AIAA/CEAS Aeroacoustics Conference*, AIAA Paper 2000-1972, 2000.

[41] Rossiter, J. E., "Wind Tunnel Experiments of the Flow over Rectangular Cavities at Subsonic and Transonic Speeds," *Ministry of Aviation; Royal Aircraft Establishment; RAE Farnborough*, 1964.

[42] Block, P. J. W., "Noise Response of Cavities of Varying Dimensions at Subsonic Speeds," NASA TN-D-8351, 1976.

M. M. Choudhari
Associate Editor